



AFRL-RH-WP-TR-2012-0206

**Toxicity Evaluation of Engineered Nanomaterials:
Portable In Vitro Chamber to Study Realistic
Occupational Exposure in Biological Systems
(Phase II Studies)**

**Saber Hussain
Bioeffects Division
Molecular Bioeffects Branch**

**Christin Grabinski
ORISE**

**Nicole Schaeublin
Elizabeth Maurer
Carol Garrett**

**Henry M. Jackson Foundation
for the Advancement of Military Medicine
Wright-Patterson AFB OH**



**Mohan Sankaran, PhD
Case Western Reserve University**

**Ravindra Pandey, PhD
Michigan Technological University**

**Jerzy Leszczynski, PhD
Jackson State University**

**William Trickler
National Center for Toxicological Research/FDA**

January 2012

Final Report for Jan 2009 – Dec 2011

**A: Approved for public release (PA);
distribution unlimited. PA Case No: 88ABW-
2012-0206 Date Cleared: 19 November 2014**

**Air Force Research Laboratory
711th Human Performance Wing
Human Effectiveness Directorate
Bioeffects Division
Molecular Bioeffects Branch
Wright-Patterson, Ohio 45433-5707**


NOTICE AND SIGNATURE PAGE

Using Government drawings, specifications, or other data included in this document for any purpose other than Government procurement does not in any way obligate the U.S. Government. The fact that the Government formulated or supplied the drawings, specifications, or other data does not license the holder or any other person or corporation; or convey any rights or permission to manufacture, use, or sell any patented invention that may relate to them.

Qualified requestors may obtain copies of this report from the Defense Technical Information Center (DTIC) (<http://www.dtic.mil>).

The experiments reported were conducted according to the "Guide for the Care and Use of Laboratory Animals," Institute of Laboratory Animal Resources, National Research Council.

(AFRL-RH-WP-TR - 2012 - 0206) has been reviewed and is approved for publication in accordance with assigned distribution statement.

**HUSSAIN.SABER.
M.1283223406**  Digitally signed by HUSSAIN.SABER.M.1283223406
DN: c=US, o=U.S. Government, ou=DoD, ou=PKI,
ou=USAF, cn=HUSSAIN.SABER.M.1283223406
Date: 2014.12.02 12:41:59 -05'00'

SABER HUSSAIN, Work Unit Manager
Molecular Bioeffects Branch

**POLHAMUS.GARRE
TT.D.1175839484**  Digitally signed by POLHAMUS.GARRETT.D.1175839484
DN: c=US, o=U.S. Government, ou=DoD, ou=PKI,
ou=USAF, cn=POLHAMUS.GARRETT.D.1175839484
Date: 2014.12.03 14:23:36 -06'00'

GARRETT D. POLHAMUS, DR-IV, DAF
Chief, Bioeffects Division
Human Effectiveness Directorate
711th Human Performance Wing
Air Force Research Laboratory

This report is published in the interest of scientific and technical information exchange, and its publication does not constitute the Government's approval or disapproval of its ideas or findings.

REPORT DOCUMENTATION PAGE			Form Approved OMB No. 0704-0188		
Public reporting burden for this collection of information is estimated to average 1 hour per response, including the time for reviewing instructions, searching existing data sources, gathering and maintaining the data needed, and completing and reviewing this collection of information. Send comments regarding this burden estimate or any other aspect of this collection of information, including suggestions for reducing this burden to Department of Defense, Washington Headquarters Services, Directorate for Information Operations and Reports (0704-0188), 1215 Jefferson Davis Highway, Suite 1204, Arlington, VA 22202-4302. Respondents should be aware that notwithstanding any other provision of law, no person shall be subject to any penalty for failing to comply with a collection of information if it does not display a currently valid OMB control number. PLEASE DO NOT RETURN YOUR FORM TO THE ABOVE ADDRESS.					
1. REPORT DATE (DD-MM-YYYY) 12-01-2012		2. REPORT TYPE Final Tech Report		3. DATES COVERED (From - To) 1-21-2009 to 12-31-2011	
4. TITLE AND SUBTITLE Toxicity Evaluation of Engineered Nanomaterials Portable In Vitro Chamber to Study Realistic Occupational Exposure in Biological Systems (Phase II Studies)			5a. CONTRACT NUMBER		
			5b. GRANT NUMBER NA		
			5c. PROGRAM ELEMENT NUMBER 62202F		
6. AUTHOR(S) Saber Hussain; Christin Grabinski; Nicole Schaeublin; Elizabeth Maurer; Carol Garrett;			5d. PROJECT NUMBER OAF		
			5e. TASK NUMBER WP		
			5f. WORK UNIT NUMBER OAFWP004		
7. PERFORMING ORGANIZATION NAME(S) AND ADDRESS(ES) 711 HPW/RHDJ 2729 R Street Wright-Patterson AFB OH 45433-5707			8. PERFORMING ORGANIZATION REPORT NUMBER		
9. SPONSORING / MONITORING AGENCY NAME(S) AND ADDRESS(ES) Air Force Materiel Command Air Force Research Laboratory 711th Human Performance Wing Human Effectiveness Directorate Bioeffects Division Molecular Bioeffects Branch Wright-Patterson AFB OH 45433-5707			10. SPONSOR/MONITOR'S ACRONYM(S) 711 HPW/RHDJ		
			11. SPONSOR/MONITOR'S REPORT NUMBER(S) AFRL-RH-WP-TR-2012-0206		
12. DISTRIBUTION / AVAILABILITY STATEMENT A: Approved for public release (PA); distribution unlimited. PA Case No: 88ABW-2012-0206 Date Cleared: 19 November 2014					
13. SUPPLEMENTARY NOTES					
14. ABSTRACT The project entitled "Toxicity Evaluation of Engineered Nanomaterials: Portable <i>In Vitro</i> Chamber to Study Realistic Occupational Exposure in Biological Systems" focused on developing a fundamental understanding of the interaction of nanomaterials (NMs) with biological molecules and provides instrumentation and field methodology design to mimic realistic exposure scenarios to predict the toxicological effects of engineered NMs upon occupational human exposure. Although many studies are being conducted to investigate the toxicity of NMs, traditional techniques do not mimic realistic exposures, which can yield contradictory and inconclusive lab experimental results. This study describes the methodology necessary for mimicking realistic NM exposure, in addition to <i>in situ</i> NM characterization and toxicity kinetics and mechanisms. The final objective is to collect relevant toxicological data to support high accuracy predictive power for human risk assessment.					
15. SUBJECT TERMS Engineered Nanomaterials, toxicity, realistic occupational exposure					
16. SECURITY CLASSIFICATION OF:			17. LIMITATION OF ABSTRACT	18. NUMBER OF PAGES	19a. NAME OF RESPONSIBLE PERSON
a. REPORT U	b. ABSTRACT	c. THIS PAGE	SAR	56	S. Hussain
			19b. TELEPHONE NUMBER NA		

THIS PAGE INTENTIONALLY LEFT BLANK.

Table of Contents

Section 1. Introduction.....	1
Section 2. Purpose	1
Section 3. Studies	1
A. Portable <i>In Vitro</i> Chamber to Study Realistic Occupational Exposure	1
B. Evaluation of Basic Toxicity of Various Metal Nanoparticles for QSAR Modeling ..	17
C. Fundamental Understanding of Biological Compatibility of Nanomaterials	28
Section 4. Publications	50

List of Tables

Table 1. Conductivity of Silver and Gold NM Dispersions.....	5
Table 2. Characterization Data for Ag NMs	8
Table 3. Predicted <i>versus</i> Experimental Results for Deposition.....	13
Table 4. Experimental Compounds Selected from the Group of Metal Oxides Based on their Experimental Crystal Lattice Parameters.....	18
Table 5. Statistical Results for Individual nano-QSAR models.....	18
Table 6. Definition of Quantum-Mechanical Descriptors	20
Table 7. Definition of Size Descriptors	21
Table 8. Results from QSAR Model.....	22
Table 9. Statistical Measures for QSAR Model.....	23
Table 10. The Calculated Structural and Electronic Properties of the Isomeric Configurations of the Trp–Au ₃₂ Complex	33
Table 11. The Calculated Structural Properties of DMTAP	44
Table 12. The Average Area per Lipid Molecule as a Function of Number of C Atoms Representing the "Tail" of a Fatty Acid	45
Table 13. The Calculated Structural Properties of DMPC and DMPE	45
Table 14. The Calculated Dipole Moments of DMPC and DMPE Monolayers.....	48

List of Figures

Figure 1. Gold nanorods dispersed in water versus media	2
Figure 2. NaviCyte horizontal diffusion chamber	3
Figure 3. Schematic of electrospray technology	4
Figure 4. Effect of serum proteins on NM conductivity and hydrodynamic diameter	5
Figure 5. Drawing of custom-designed heat plate.....	6

Figure 6. Image showing the internal features of the chamber	6
Figure 7. Modified chamber	7
Figure 8. Darkfield images showing Au 60 nm particle deposition on glass coverslips after 30 min generation by electro spray	8
Figure 9. TEM image of Ag NMs	8
Figure 10. Ag NMs (40 nm) stabilized with citrate were sprayed at a concentration of 20 µg/mL with electro spray settings of 1.45 kV (38 nA) and diluted in either air (A) or nitrogen (B).....	9
Figure 11. Uniform deposition of Ag NMs electro sprayed from a dispersion at 1 mg/mL and diluted in nitrogen + 5% CO ₂	10
Figure 12. A549 cells embedded in resin, sectioned, and imaged using TEM	10
Figure 13. Ag NMs (60 nm) stabilized with citrate were sprayed at a concentration of 20 µg/mL with electro spray settings of 1.45 kV (38 nA).....	11
Figure 14. MPPD results for total mass per area as a function of airway generation number for Ag 60 nm and 40 nm	12
Figure 15. Cell viability data for cells grown in the chamber for 30 minutes with an electric field of 2kV/cm versus cells grown at the air liquid interface in an incubator.....	14
Figure 16. Poster presented at the SOT conference on 13 March 2012.....	15
Figure 17. Multi-chamber model	16
Figure 18. Williams plot describing applicability domains of GA-MLR model	23
Figure 19. A visual correlation between the experimental and predicted values of log (1/EC ₅₀).....	24
Figure 20. Poster presented at the SOT conference on 13 March 2012.....	25
Figure 21. Generation of ROS after 4h exposure to MeONPs	27
Figure 22. The calculated ground state configurations and total charge density of (a) (Au ₃₂), and (b) Trp	31
Figure 23. The ground state configurations of Trp–Au ₃₂ complex.....	32
Figure 24. Total charge density plot of Au ₃₂ , Trp and isomeric configurations of Trp–Au ₃₂ complex projected along (001) plane.....	35
Figure 25. The contour plots of molecular orbitals of pristine Trp, Au ₃₂ and Trp–Au ₃₂ conjugate isomers shown at 1/2nd of its maximum isosurface value.....	36
Figure 26. Density of states of Trp, Au ₃₂ and Trp–Au ₃₂ complex isomers.....	37
Figure 27. The projected density of states (PDOS) of interacting atoms.....	39
Figure 28. A ball and stick model for DMTAP	43
Figure 29. A ball and stick model for DMTAP layer.....	43
Figure 30. A ball and stick model for DMPC layer	44

Figure 31. A ball and stick model for DMPE layer..... 45
Figure 32. The electron density contour plots of DMPC 46
Figure 33. The electron density contour plots of DMPE..... 47
Figure 34. A ball and stick model for the DMPC: H₂O system 47
Figure 35. A ball and stick model for the DMPC: H₂O system 48

Section I. Introduction

The project entitled “Toxicity Evaluation of Engineered Nanomaterials: Portable *In Vitro* Chamber to Study Realistic Occupational Exposure in Biological Systems” focused toward developing a fundamental understanding of the interaction of nanomaterials (NMs) with biological molecules and developing the instrumentation and methodology to mimic realistic exposure scenarios to predict the toxicological effects of engineered NMs in relation to occupational human exposure. Dr. Saber Hussain was the overall program manager as well as a Principal Investigator.

Section II. Purpose

The research gap to develop realistic ambient NM exposure scenarios in nanotoxicology was addressed. Although many studies are being conducted to investigate the toxicity of NMs, traditional techniques do not accurately mimic material characteristics during exposure, which can yield contradictory and inconclusive results in laboratory NM testing experiments. This study describes the methodology necessary to develop more realistic NM exposure conditions, in addition to providing aspects of *in situ* NM characterization and toxicity kinetics and mechanisms. The final objective is to collect relevant toxicological data to support accurate data gathering for high predictive power during human exposures risk assessment.

Section III. Studies

A. Portable *In Vitro* Chamber to Study Realistic Occupational Exposure in Biological Systems

Studies conducted by Ms. Christin Grabinski, MS

The main objective of this study was to design an experimental set-up, incorporating engineered NM aerosolization and *in vitro* exposure at the air-liquid interface, to mimic realistic respiratory inhalation conditions. Traditional exposure testing begins with a series of *in vitro* assessments that commonly require engineered NMs be dispersed in biological media prior to exposure. This approach can alter the NMs physical properties (e.g. agglomeration) and chemical surface (e.g. protein coating). There are many examples of agglomeration tendency for NM, but even the dynamics can be changed; for example mercaptohexadecanoic acid functionalized gold nanorods, which are stable when dispersed in water, but become very unstable when dispersed at the same concentration in media (Figure 1). Because many nanoparticles agglomerate in biological media without the addition of a surface stabilizing molecule, we recognized that mimicking realistic exposure conditions in the lab is difficult and will produce unique results from traditional techniques. Consequently, lab model procedures and systems for NM exposures require a redesign to more accurately assess human risk.

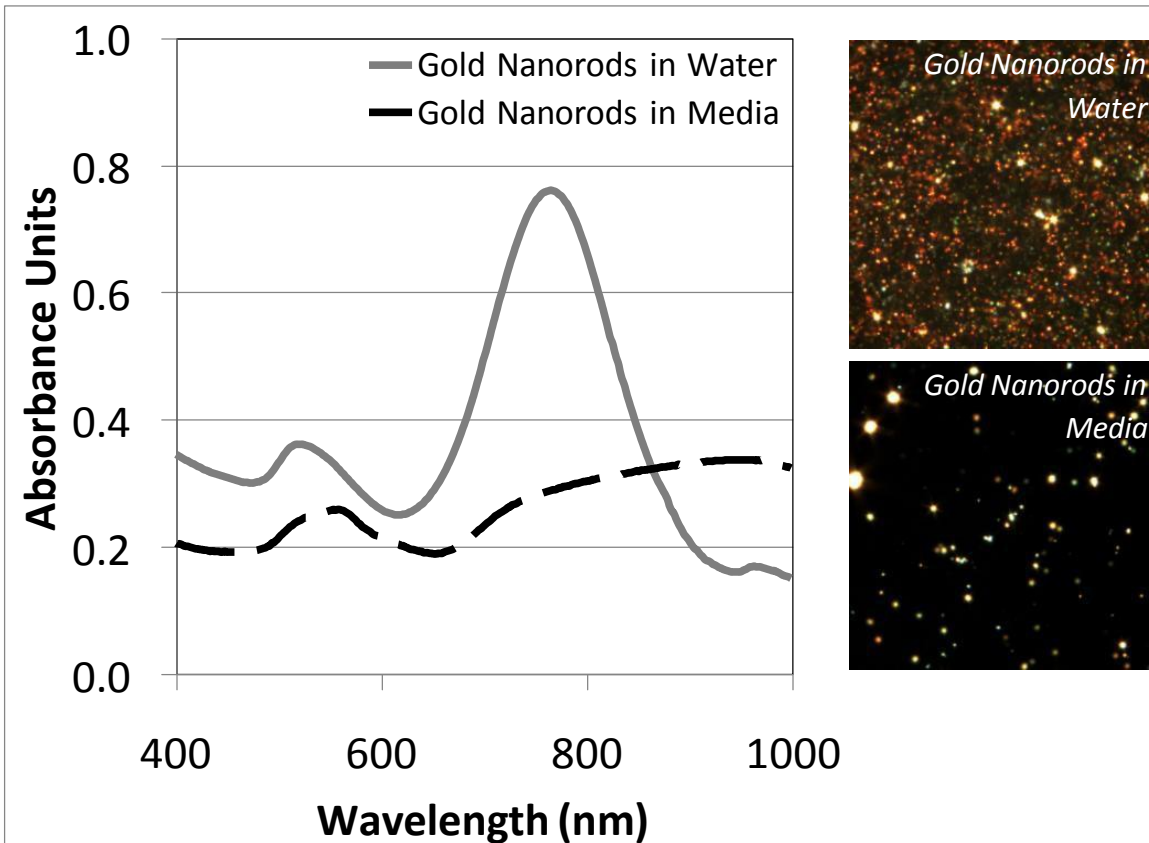


Figure 1. Gold nanorods dispersed in water versus media. Plot: UV/Vis data exhibited a flattened longitudinal peak for gold nanorods dispersed in media indicating significant agglomeration. Insets: Darkfield images confirm this phenomenon visually. This figure was modified from Grabinski et al. (2011) [1].

In order to address this challenge, an instrument set-up was designed and engineered for exposing cells, grown on a biocompatible membrane with the cell surface side toward the environment, to ambient NMs dispersed in the gas phase. For our pilot experiments, a commercially available horizontal NaviCyte chamber (Warner Instruments) was used as a closed environment to expose gas-phased, engineered NMs to eukaryotic cells, grown on a 0.4 micron porous membrane insert (Corning) (Figure 2).

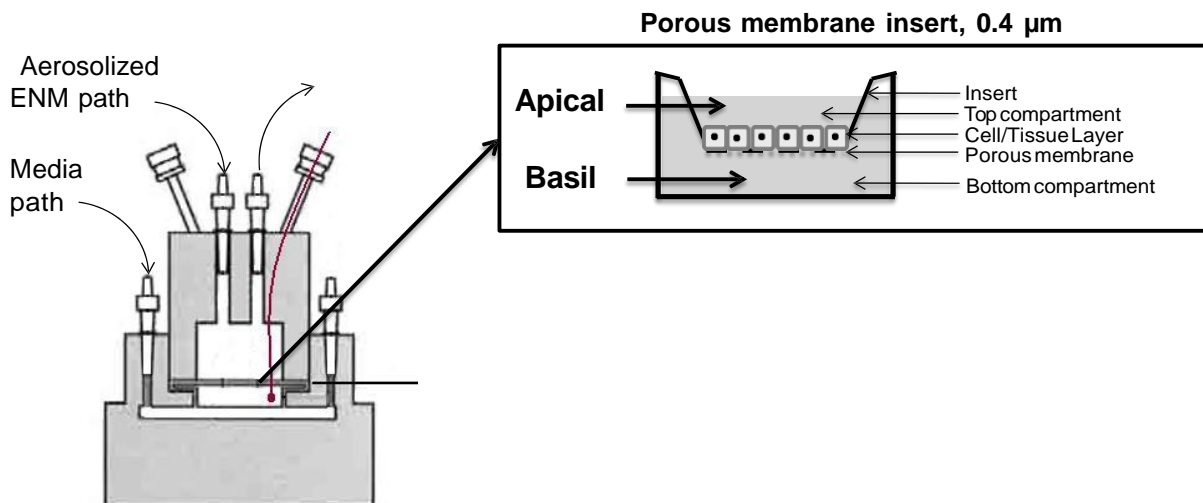


Figure 2. NaviCyte horizontal diffusion chamber for air-liquid exposure with porous membrane insert. Image of the chamber was modified from Warner Instruments Catalogue "A Guide to Ussing Chamber Systems." pp. 9-10. Available at https://www.harvardapparatus.com/hapdfs/HAI_DOCCAT_4/Ussing_Chamber_Systems.pdf

Different techniques were used for dispersing engineered NMs in the gas phase. For the first phase of the project, engineered NMs were dispersed using electro spray techniques (TSI, Shoreview, MN). The electro spray operates by drawing a conductive buffer containing dispersed engineered NMs into a capillary. An electric field is applied, drawing the liquid into a conical jet, which releases ultrafine charged droplets. For dilute liquid dispersions, each droplet contains a small number of NMs, allowing for uniform gas phase dispersion. Once droplets containing NMs are formed, the liquid evaporates leaving particles in the gas phase. The charge on the NMs is neutralized by a sealed ionizing source (Polonium-210). The particles are then mixed with a flow of filtered dry air (95%) and CO₂ (5%), which can then be directed to the exposure chamber (Figure 3). Future studies will investigate additional approaches for NM aerosolization, including aerosolization of dry powders and direct synthesis in the aerosol phase. For the latter, metal, carbon, and semiconductor NMs will be synthesized in the gas phase using direct current atmospheric-pressure microplasma, which has been standardized by Dr. Mohan Sankaran of Case Western Reserve University [2].

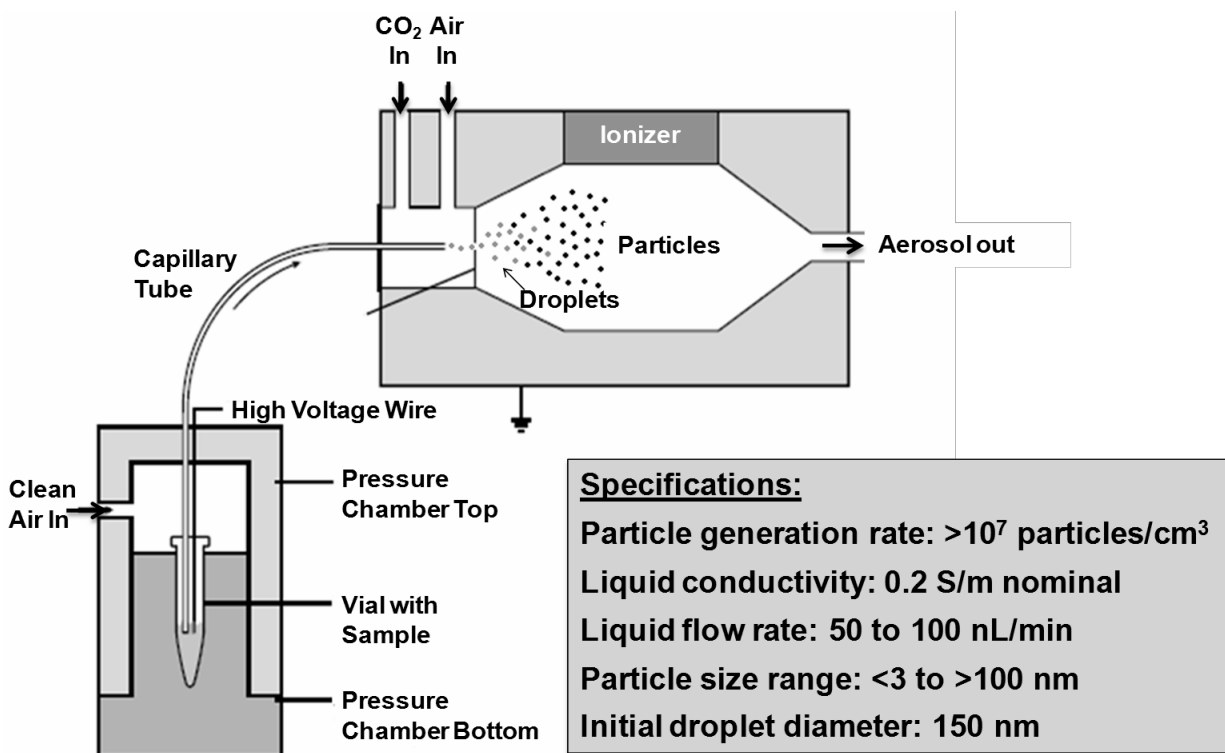


Figure 3. Schematic of Electro spray technology.

Schematic was modified from: Product Information sheet. "Model 3480 Electro spray Aerosol Generator", P/N 1930098 Rev A. Copyright © 2001 TSI Incorporated Printed in U.S.A. (091401 - - PDF updated 012902). Available at: http://www.tsi.com/uploadedFiles/Product_Information/Literature/Spec_Sheets/3480.pdf

One of the key features of this technique is the requirement for a conductive dispersion. The manufacturer recommends a conductivity of 2000 μ S/cm for drawing NMs from a liquid dispersion using cone-jet mode. We found that it is very difficult to reach this level of conductivity for stable dispersions of gold and silver NMs. However, it is possible to generate NM aerosols using lower conductivity dispersions in silver bullet mode, which has also been shown to be a stable approach for generating aerosols [3]. For both gold and silver NMs, the conductivity is high enough to achieve silver-bullet mode. The results for various NM dispersions are shown in Table 1. Silver (Ag) NM dispersions exhibit a higher conductivity relative to gold (Au) NMs in the same stabilizing agent. This is due to the greater propensity for Ag to oxidize in solution and produce Ag ions [4]. Au NMs stabilized with tannic acid exhibit a much lower conductivity. Also, it was shown that serum proteins could be added to increase the conductivity (Figure 4). Serum proteins are typically used in cell culture media, so they are preferred over typical buffers, such as ammonium acetate, which can affect cytotoxicity at low exposure levels. In addition to an increase in the conductivity, serum proteins slightly increase the hydrodynamic diameter due to adsorption onto the surface of the NMs. However, this increase reaches a maximum value at around 4% serum (Figure 4B).

Table 1. Conductivity of Silver and Gold NM Dispersions

Nanomaterial	Stabilizing Agent	Concentration (mg/mL)	Conductivity ($\mu\text{S}/\text{cm}$)
Ag, 60 nm	Citrate	0.02	660
Au, 60 nm	Citrate	0.02	197
Au, 60 nm	Tannic acid	0.02	120

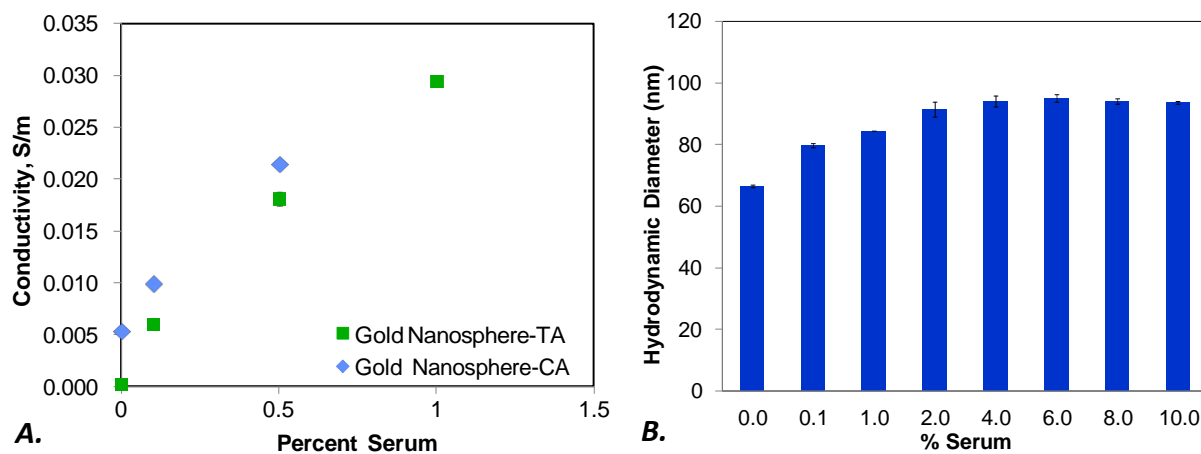


Figure 4. Effect of serum proteins on NM conductivity and hydrodynamic diameter. A. Conductivity increases with increasing serum; B. Hydrodynamic increases with increasing serum due to protein adsorption.

In order to incorporate the electrospray with the exposure chamber, the outlet of the electrospray was connected to the chamber, with the remaining flow directed into a HEPA filter (TSI). Since the cells are sensitive to flow, the flow rate into the chamber was controlled using a vacuum pump and mass flow meter (TSI 4140). A heat plate was used to maintain the internal chamber of the system at 37°C using a TC-324B dual channel controller (Warning Instruments). The heat plate was custom designed by Frazier Nash to incorporate connections for thermocouples and secure fitting of the NaviCyte chamber (Figure 5). Within the chamber, cells were grown on Snapwell membranes (Corning) and fed with media on the basal side, then exposed to air on the apical side (Figure 6). The outlet of the chamber was connected to a HEPA filter (TSI) to prevent release of NMs into the environment.

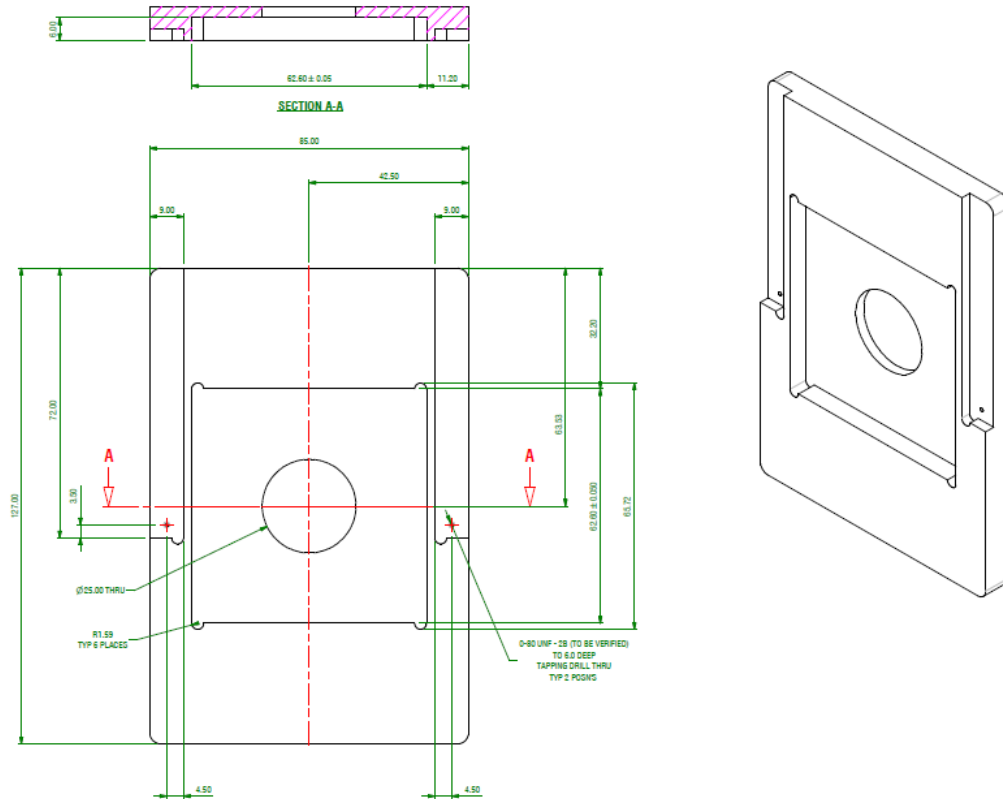


Figure 5. Drawing of custom-designed heat plate for controlling the temperature of the NaviCyte chamber.

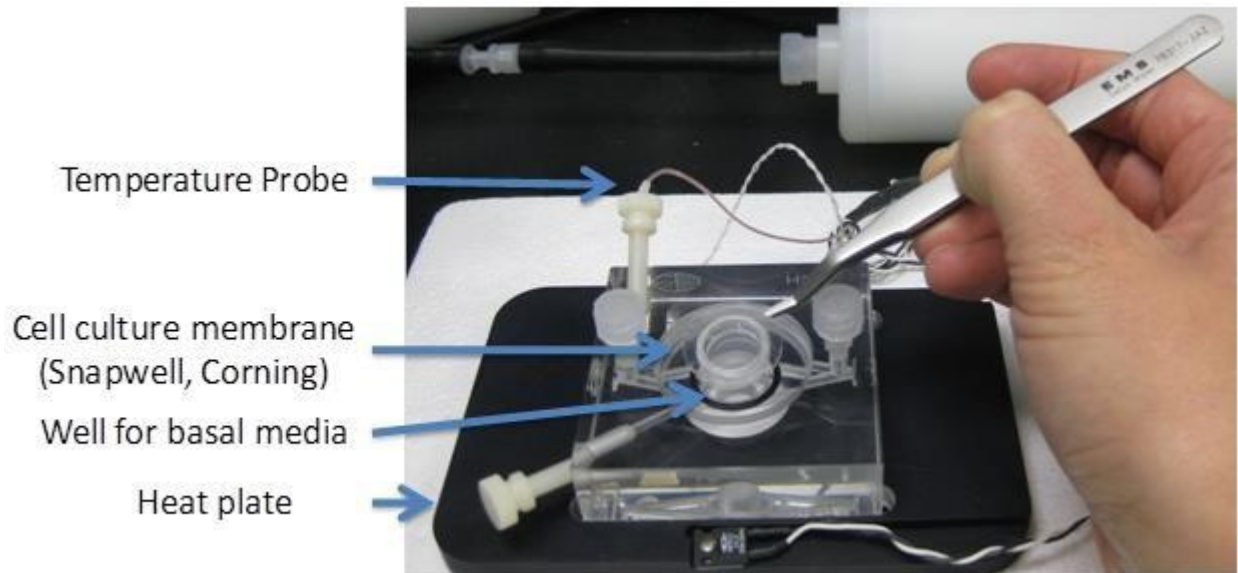
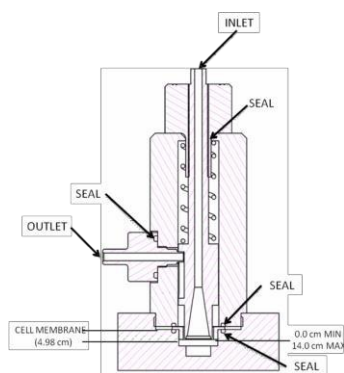


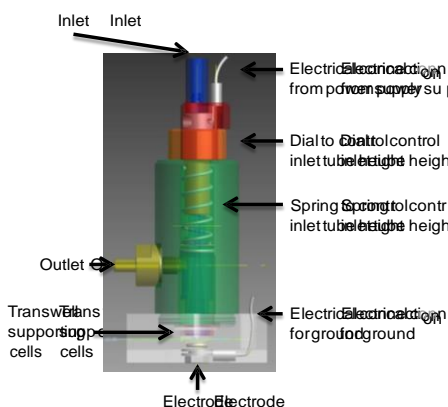
Figure 6. Image showing the internal features of the chamber.

In order to control the deposition of NMs onto the cells in the chamber, it was necessary to modify the chamber. The design allows for an electric field to be applied using an external power source for electrostatic deposition of NMs. Adjustment of the inlet tube to create from 0 to 14 cm distance between the end of the tube and cell membrane allows for the effect of distance on the electric field and deposition efficiency to be optimized. This height adjustment was facilitated by a spring mechanism around the inlet tube. An electrode was attached to the inlet tube and a conducting material placed below the cell membrane. The inlet tube and springs for adjusting the height are 316 stainless steel (SS) and completely enclosed within the system, while the majority of the chamber was constructed using polycarbonate (Figure 7).

2-Dimensional Drawing



3-Dimensional Model



Prototype

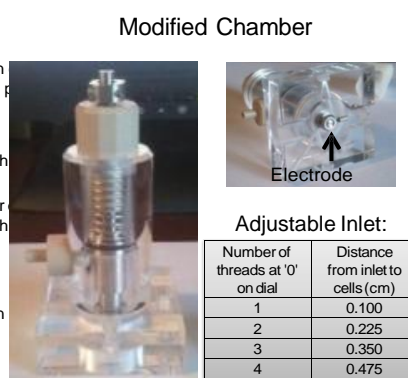


Figure 7. Modified Chamber. A drawing and three-dimensional model were developed, and the prototype was machined based on this model. The key features include the adjustable inlet tube and insertion of electrodes, which will allow for application of an electric field and dose control.

NM deposition was optimized using the electro spray to draw NMs into the gas phase and electrostatic deposition (Nanometer Aerosol Sampler) to deposit them onto glass coverslips. Electro spray generation and NM deposition was investigated for Au 60 nm particles. Greater than 6x more uptake was observed for NM deposition using electrostatic deposition, verifying the application of an electric field increases deposition efficiency (Figure 8).

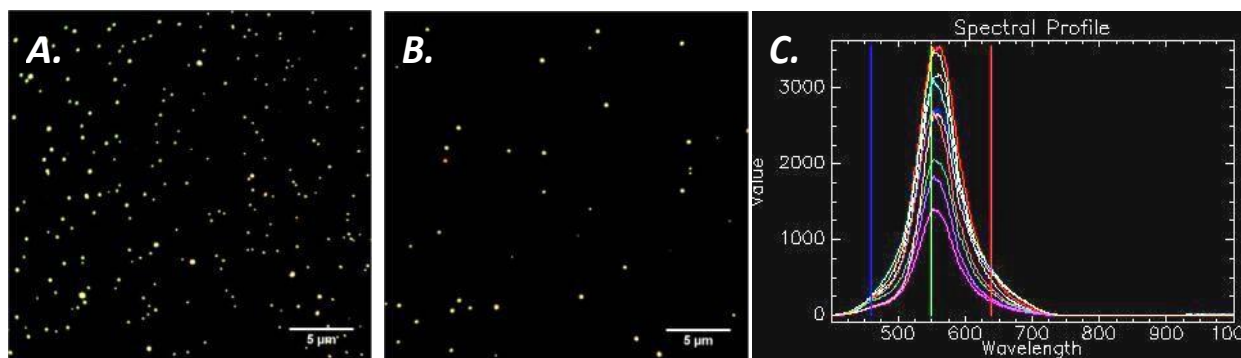


Figure 8. Darkfield images showing Au 60 nm particle deposition on glass coverslips after 30 min generation by electro spray (1.7 kV; -066 nA). A. NAS (~10,000 kV); B. Chamber (0 kV); C. Spectral data for illuminated spots.

Another set of experiments were conducted using Ag NMs. Ag NMs (Ted Pella, Inc.) were characterized before aerosolization and deposition using transmission electron microscopy (TEM) and ImageJ for primary particle size. They were found to exhibit an average primary particle size of 41.56 nm (Figure 9; Table 2). Dynamic light scattering (DLS) was used to determine the hydrodynamic diameter, which was found to be 42.44 nm (Table 2).

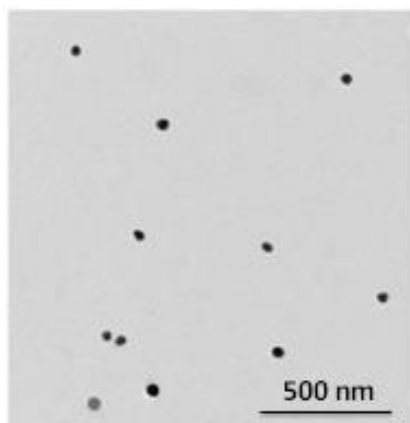


Figure 9. TEM image of Ag NMs.

The zeta potential of the Ag NM solution was -43.6 mV, indicating stable dispersion (Table 2). The conductivity of the Ag NM solution was 300 $\mu\text{S}/\text{cm}$ (Table 2).

Table 2. Characterization Data for Ag NMs

Primary Diameter (nm)	Hydrodynamic Diameter (nm)	Zeta Potential (mV)	Conductivity ($\mu\text{S}/\text{cm}$)
41.56 \pm 6.76	42.44 \pm 0.18	-43.6 \pm 5.2	300

The conductivity was sufficient to allow for steady operation of the electrospray at 1.45 kV (-40 nA) and 1.05 LPM flow (~95% air; 5% CO₂). Ag NMs (~40 nm) were aerosolized using electrospray in either an oxygen or nitrogen environment and deposited onto TEM grids in the presence of an electric field (-10 kV). The results showed that aerosolization in an oxygen environment significantly altered the morphology (Figure 10). The use of nitrogen gas for diluting aerosolized NMs does not alter the morphology.

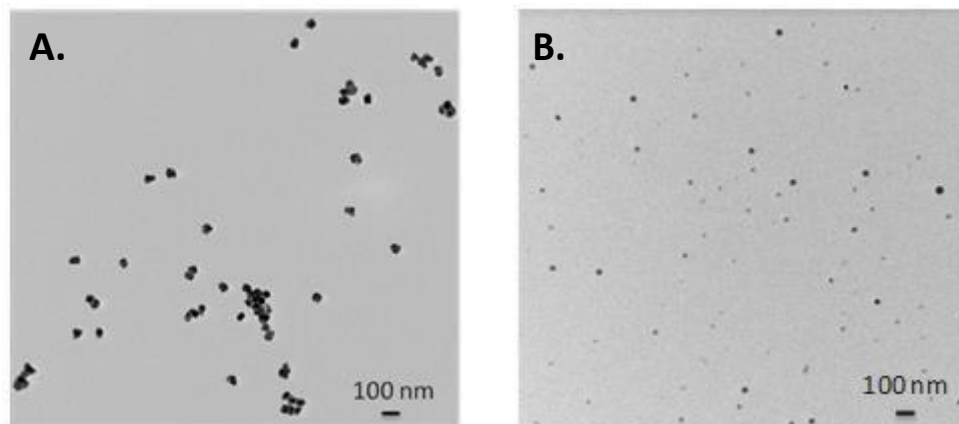


Figure 10. Ag NMs (40 nm) stabilized with citrate were sprayed at a concentration of 20 $\mu\text{g/mL}$ with electrospray settings of 1.45 kV (38 nA) and diluted in either air (A) or nitrogen (B).

For cytotoxicity studies, it is desired to achieve even deposition of NMs. Therefore, Ag NMs (nanoComposix; 1 mg/mL) were aerosolized using electrospray (and diluted in nitrogen), and the deposition was investigated using the Nanometer Aerosol Sampler with maximum DC voltage (~ -10 kV; 1.8-1.9 kV/cm). The deposition was investigated throughout the TEM grid and found to represent equivalent dose without statistically significance differences for particles counted in the middle, center and edge capture regions. A total of 10 TEM images were analyzed in order to collect the data displayed in Figure 11. The particles/cm² concentrations were calculated using ImageJ software.

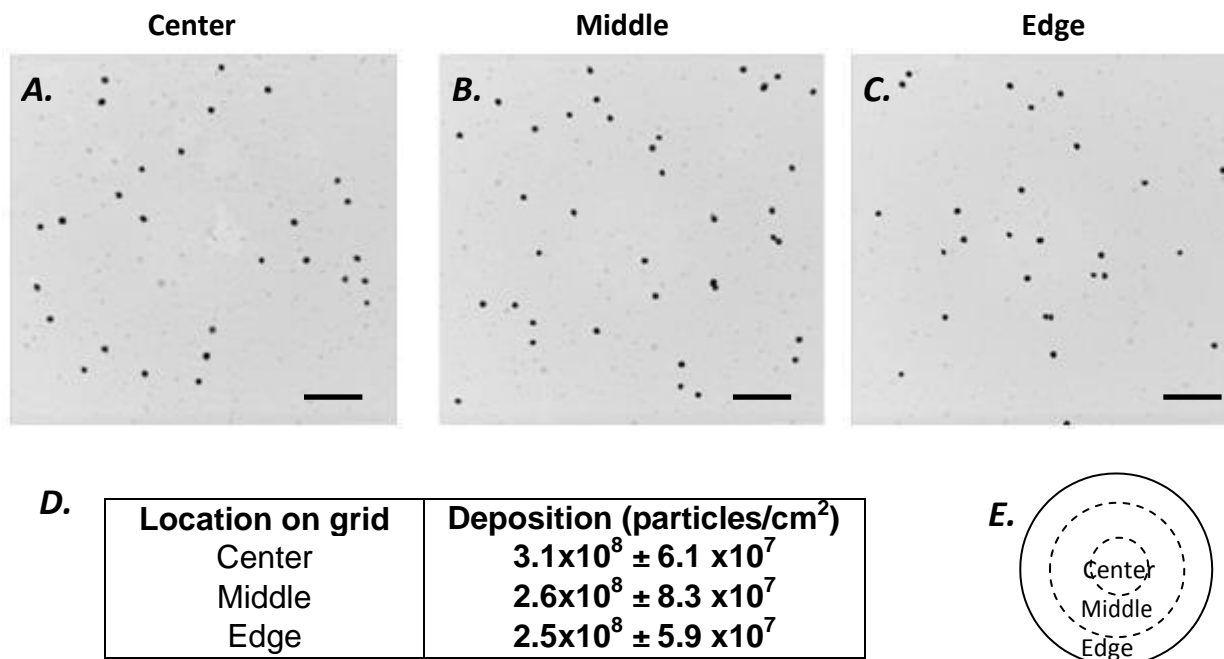


Figure 11. Uniform deposition of Ag NMs electro sprayed from a dispersion at 1 mg/mL and diluted in nitrogen + 5% CO₂. A-C. TEM images from the center (A), middle (B), and edge (C) of the grid. D. Table showing data collected from 10 images representing the different parts of the TEM grid (scale bar represents 500 nm); E. Schematic to explain words used for describing deposition throughout the grid.

Before initiating experiments with cells, A549 immortalized lung epithelial cells were grown on a 12 mm membrane insert for 7 days and imaged to verify confluence. A cross-section of the cells imaged using TEM are shown in Figure 12.

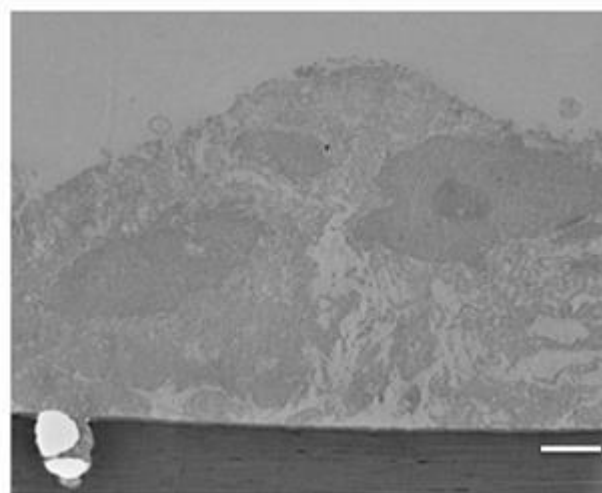


Figure 12. A549 cells embedded in resin, sectioned, and imaged using TEM. The scale bar corresponds to 2 μm.

NM deposition onto cells was investigated using Ag NMs with diameter of 40 and 60 nm from Ted Pella, Inc. (Redding, CA). Particles were delivered to the modified chamber containing A549 cells. After exposure, the cells were washed, and then trypsinized, and the amount of Ag in the wash solution and cells was quantified using Inductively Coupled Plasma Mass Spectrometry (ICP-MS). The number of Ag particles was calculated based on the density of Ag and estimated volume for the respective Ag nanoparticle sizes. The deposition of 40 nm Ag particles was significantly higher than 60 nm Ag particles (Figure 13). This observation was expected based on the higher diffusion rate for smaller particles.

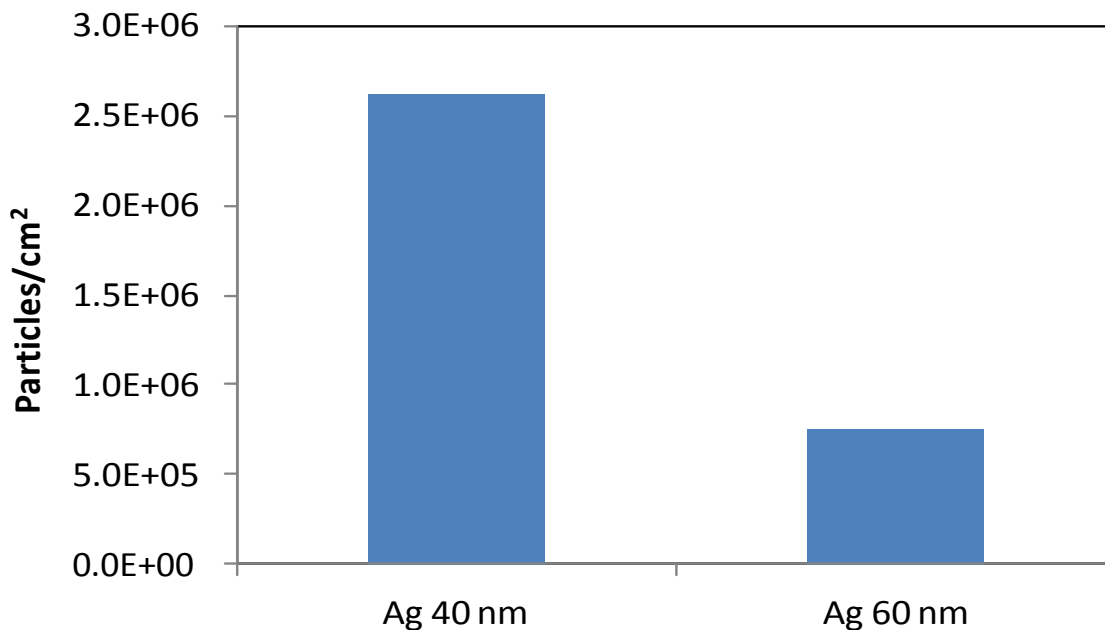
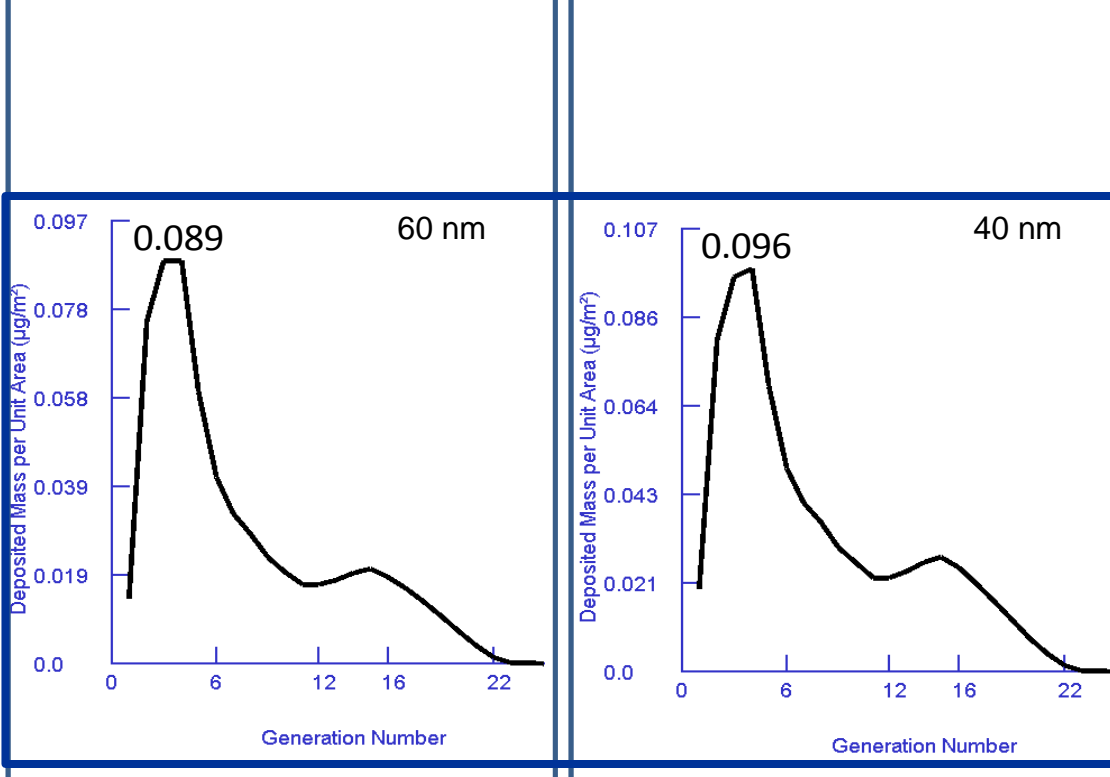


Figure 13. Ag NMs (60 nm) stabilized with citrate were sprayed at a concentration of 20 $\mu\text{g/mL}$ with electrospray settings of 1.45 kV (38 nA).

The ICP-MS results were compared to results obtained using the Multiple Path Particle Dosimetry (MPPD) model for a 6 hour exposure. MPPD calculates deposition & clearance of aerosols in all airways of the lung. It is based on published theoretical efficiencies for deposition and considers filtration by the nose and mouth [5]. The MPPD input includes spherical Ag particles (40 or 60 nm), human airway geometry, and initial concentration of 0.1 mg/m^3 , which is the exposure limit for silver dust set by the American Conference of Governmental Industrial Hygienists [6]. The data is for 1 breath (assume 12 breaths/min). The results obtained using the Multiple Path Particle Deposition model is shown in Figure 14.



0.120

Figure 14. MPPD results for total mass per area as a function of airway generation number for Ag 60 nm and 40 nm.

Assuming 12 breaths/minute, the concentration can be adjusted to a 6 h exposure (Equation 1). These data can be adjusted to get the total mass deposited (M_{dep}) for any exposure time (t), as shown in equation 1. Also, it can be converted to particles per surface area (N_{dep}) using the particle volume (V) and density (ρ), as shown in Equation 2. To determine what the equivalent exposure would be in a traditional culture system, equation 3 can be used. The deposition efficiency (ϵ_{dep}) is a function of NM transport in culture media. It can be derived using published theoretical predictions for gravitational settling and diffusion of NM agglomerates [7].

$$p \left[\frac{\mu}{\text{---}} \right] = \frac{PPD \left[\frac{\mu}{\text{---}} \right] * \left[\frac{\text{---}}{\text{---}} \right] * \left[\frac{\text{---}}{\text{---}} \right]}{\left[\frac{\text{---}}{\text{---}} \right]} \quad \text{Equation 1}$$

$$p \left[\frac{p}{\text{---}} \right] = \frac{p \left[\frac{\mu}{\text{---}} \right]}{\rho \left[\frac{\text{---}}{\text{---}} \right] * \left[\frac{\mu}{\text{---}} \right] * V \left[\frac{\text{---}}{\text{---}} \right]} \quad \text{Equation 2}$$

$$xp \left[\frac{\mu}{\text{---}} \right] = \epsilon_p \quad \text{Equation 3}$$

Table 3. Predicted versus Experimental Results for Deposition.

Sample	N_{dep} (particles/cm ²)	
	Predicted	Experimental
Ag 40 nm	$2.4 \times 10^6 - 1.1 \times 10^7$	2.6×10^6
Ag 60 nm	$6.4 \times 10^5 - 3.0 \times 10^6$	5.9×10^5

The experimental deposition was lower than the estimated realistic maximum dose (Table 3). It is proposed that higher doses can be obtained by generating an electric field in the chamber. The final outcome of incorporating the MPPD model and dosimetry approximations for dosing and exposure of NMs is expected to produce realistic results for NM toxicity *in vitro*, which to our knowledge have not yet been produced in one complete study. Results from conventional dosing at the air-liquid interface (*via* dispersion of NMs in the culture media) will be completed for comparison to aerosol exposure.

Based on an extensive review of literature and discussion with collaborators, we discovered that a critical gap in the literature that includes limited research regarding the optimal electric field strength and frequency for depositing NMs. Therefore, we purchased a function generator and power amplifier where these instruments can be applied to work together to adjust the voltage and frequency coming from the electrical outlet, and then amplify the signal to the range necessary for electrostatic deposition. When voltage is applied using the power supply, the electric field is achieved between the end of the inlet tube and the electrode underneath the cell membrane. The inlet tube was fitted with a fine metal mesh to allow for an even field to be applied across the cell membrane. Due to the arrangement of the set-up, there is negligibly low electrical current on the cell cultures. Deposited NMs would yield a current measured in femto-amps which was 10^{17} times lower than currents used to induce cell damage through electroporation [8].

In order to investigate the effect of the electric field on cell survival, cells were grown for 30 minutes in the chamber with the electric field set to 2 kV/cm. The Alamar Blue assay was used to assess viability of cells in the chamber *versus* cells grown at the air liquid interface in the incubator. There was no negative effect observed (Figure 16). Therefore, the power supply has been successfully integrated with the chamber, and cell viability was not affected by exposure to the electric field.

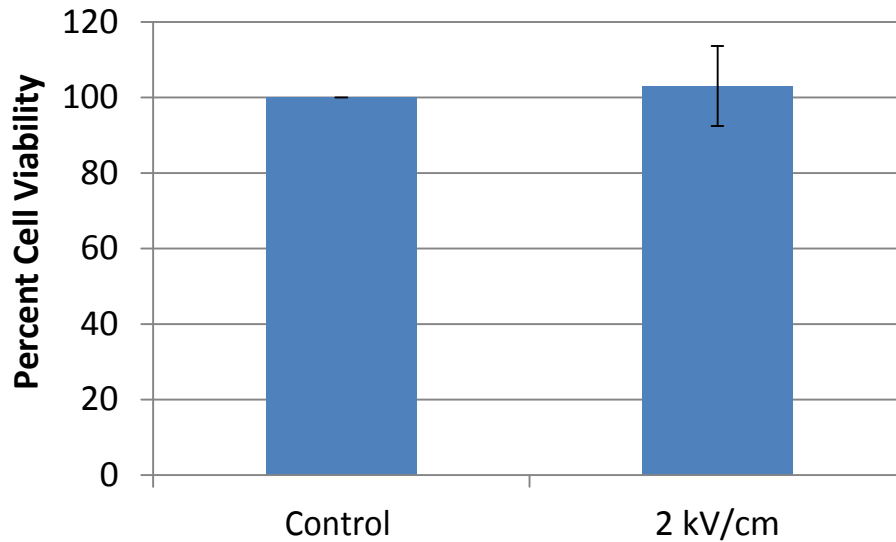


Figure 15. Cell viability data for cells grown in the chamber for 30 minutes with a electric field of 2kV/cm versus cells grown at the air liquid interface in an incubator. Samples were tested in triplicate. A student's t-test revealed that there is no statistical difference between the control and test sample.

This project was presented during a poster session at the Society of Toxicology meeting in San Francisco on 13 March 2012. The poster is shown on the next page (Figure 16).



Design of an *In Vitro* Chamber for Occupational Exposure Assessment of NMs



Christin Grabinski^{1,2}, Mohan Sankaran², and Saber M. Hussain¹
¹711 HPW/RHDJ, Air Force Research Laboratory, Wright-Patterson AFB, OH
²Department of Chemical Engineering, Case Western Reserve University, Cleveland, OH

Background

Nanomaterials (NMs) are being implemented in many Air Force applications, such as fuels, weapons, and sensors. Inhalation is the key route of concern for occupational exposure to NMs.

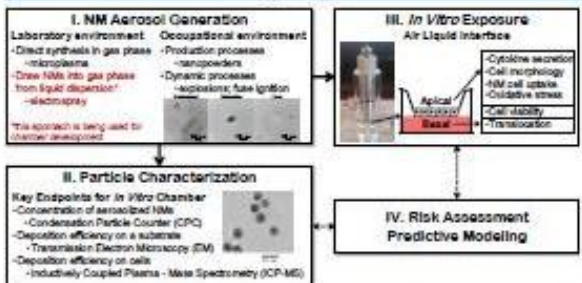


Traditional *in vitro* toxicity assays require that NMs are dispersed in biological media prior to exposure, which can alter their properties and does not mimic realistic exposure (Grabinski et al., 2011; Hussain et al., 2009). Therefore, it is critical to develop methods for exposing cells to NMs dispersed in the gas phase.

Objective

The objective is to develop the instrumentation and methodology for exposing aerosolized NMs to cells grown at the air liquid interface.

Approach



Experimental Set-up

A commercial electrospay (TSI, Shoreview, MN) was used for particle dispersion in the gas phase due to the ability for controlled generation of monodisperse NMs and ability to use liquid NM dispersions of interest. A CPC was used to measure the concentration of particles exiting the electrospay, a modified horizontal diffusion chamber to maintain cells at the air liquid interface, a heat plate to maintain internal temperature of the chamber, and an AC power supply for electrostatic deposition of NMs in the chamber. The experimental set-up is shown below:



Results

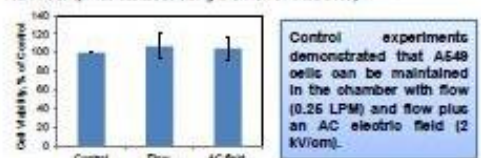
Cell Viability and Morphology

A human lung epithelial cell-line (A549) was used to validate the ability for cells to be maintained in the modified chamber. A549 cells were seeded on a porous polyester membrane and grown to form a confluent monolayer as previously described (Rothen-Rutishauser et al., 2009). The membranes were fixed, dehydrated and sectioned for TEM to verify the monolayer formation.



TEM image of a transverse section of the membrane verified that A549 cells formed a confluent layer.

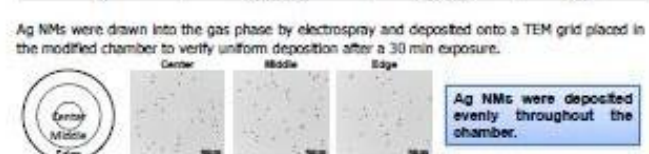
A549 cells were grown in the modified chamber and exposed to gas flow (95% N₂, 5% CO₂) at a rate of 0.25 liters per minute (LPM) for 30 min. Cell viability was assessed using the Alamar Blue assay.



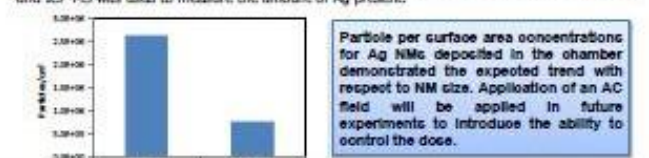
Control experiments demonstrated that A549 cells can be maintained in the chamber with flow (0.25 LPM) and flow plus an AC electric field (2 kV/cm).

NM Deposition

Experiments were conducted to verify NM deposition in the modified chamber. Ag NM dispersions (40 & 60 nm; Ted Pella) were characterized via dynamic light scattering (DLS) and Laser Doppler Electrophoresis (LDE).



Ag NMs were drawn into the gas phase by electrospay and deposited onto A549 cells grown in the chamber for 30 min. After exposure, the cells were trypsinized from the membrane inserts, and ICP-MS was used to measure the amount of Ag present.

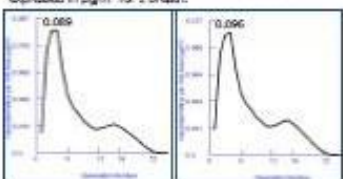


Particle per surface area concentrations for Ag NMs deposited in the chamber demonstrated the expected trend with respect to NM size. Application of an AC field will be applied in future experiments to introduce the ability to control the dose.

Dose Validation

Multiple Path Particle Dosimetry Model (MPPD) was used to predict a realistic dose for inhalation exposure of Ag NMs. The model is based on published theoretical efficiencies for particle deposition (Anjilvel, 1995).

MPPD Input: Ag NMs (40 & 60 nm); human airway geometry; concentration of 0.1 mg/m³ (recommended exposure limit for Ag dust; Lee et al., 2011). Data is expressed in µg/m³ for 1 breath.



The deposited mass per surface area (M_{depos}) can be calculated for a defined exposure time (t) and used to estimate realistic exposures for the *in vitro* chamber (Equation 1). The deposited particle number (N_{depos}) can be calculated from the deposited mass, and is a function of the particle volume (V_{part}) and density (ρ) (Equation 2).

$$M_{depos} \left[\frac{kg}{cm^2} \right] = \frac{MPPD \left[\frac{kg}{m^3} \right] \cdot A_{chamber} \left[m^2 \right] \cdot t \left[\frac{min}{60} \right]}{V_{chamber} \left[m^3 \right] \cdot 1000 \left[\frac{cm^3}{m^3} \right]} \quad \text{Equation 1}$$

$$N_{depos} \left[\frac{particles}{cm^2} \right] = \frac{M_{depos} \left[\frac{kg}{cm^2} \right]}{\rho \left[\frac{kg}{cm^3} \right] \cdot 1000 \left[\frac{cm^3}{m^3} \right]} \cdot \frac{V_{part} \left[m^3 \right]}{V_{part} \left[m^3 \right]} \quad \text{Equation 2}$$

The particle per surface area concentration range predicted by the MPPD model was calculated for a 30 minute exposure using equations 1 and 2. The particle per surface area concentration determined by ICP-MS measurement are reported in the table for comparison.

Sample	N_{depos} (particles/cm ²)	
	Predicted	Experimental
Ag 40 nm	2.6×10^8	2.6×10^8
Ag 60 nm	5.9×10^8	5.9×10^8

The experimental values are on the order of magnitude predicted by the MPPD model.

Conclusion and Future Work

The results of this study demonstrate that the current experimental set-up can be used as a realistic approach for assessing inhalation toxicity of aerosolized NMs *in vitro*. Future work will be performed to optimize NM dose as a function of AC electric field strength for controlled dose. Additionally, a multi-chamber instrument is currently being designed to allow for collection of statistical data. The multi-chamber instrument will be portable for use in both laboratory and occupational environments.

Acknowledgements

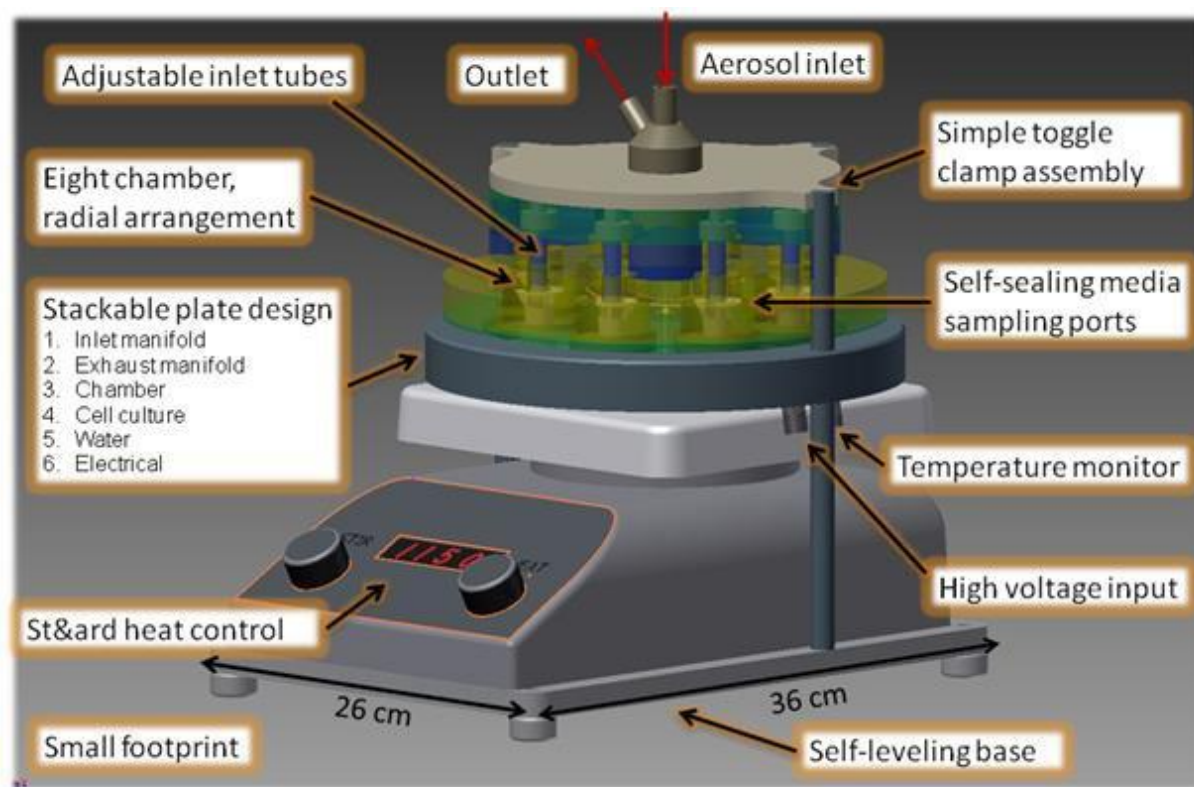
This work is funded through the Office of the Air Force Surgeon General. Ms. Grabinski receives a fellowship from the Oak Ridge Institute for Science and Education. We thank Dr. Seung Lee (Case Western Reserve University) for his help building the AC power supply and Ms. Elizabeth Maurer (Air Force Research Laboratory) for analyzing ICP-MS samples.

References

Hussain et al. *Air. Mater.* 2006, 22, 1540-50.
Grabinski et al. *ACS Nano* 2011, 5, 2870-9.
Rothen-Rutishauser. *Environ. Sci. Technol.* 2009, 43, 2634-40.
Lee et al. *Environ. Toxicol.* 2011, 4, 228-36.
Anjilvel and Aaghaer. *Respirat. Appl. Toxicol.* 1995, 7, 41-50.

Figure 16. Poster presented at the SOT conference on 13 March 2012.

Based on the success with the prototype chamber, a scaled-up multi-chamber was designed. A schematic of the scaled up chamber is shown in figure 17.



Model images provided by Frazer-Nash USA modeled in Inventor

Figure 17. Multi-chamber model

References

- [1] Grabinski, C.; Schaeublin, N.; Wijaya, A.; D' Couto, H.; Baxamusa, S.H.; Hamad-Schifferli, K.; Hussain, S.M. *ACS Nano* **2011**, *26*, 2870-2879.
- [2] Chiang, W.H.; Sankaran, R.M. *Appl. Phys. Lett.* **2007**, *91*, 121503(1-3).
- [3] Chen, D.R.; Pui, D.Y.H.; Kaufman, S.L. *J. Aerosol Sci.* **1995**, *26*, 963-977.
- [4] Levard, C.; Hotze, E.M.; Lowry, G.V.; Brown, G.E. *Environ. Sci. Technol.* **2012**, *46*, 6900-6914.
- [5] Anjilvel, S.; Asgharian, B. *Fundam. Appl. Toxicol.* **1995**, *28*, 41-50.
- [6] Lee, J.H.; Kwon, M.; Kang, C.S.; Ahn, K.H.; Han, J.H.; Yu, I.J. *Inhal. Toxicol.* **2011**, *4*, 226-236.
- [7] Teeguarden, J.G.; Hinderliter, P.M.; Orr, G.; Thrall, B.D.; Pounds, J.G. *Toxicol. Sci.* **2007**, *95*, 300-312.
- [8] Savi, M.; Kalberer, M.; Lang, D.; Ryser, M.; Fierz, M.; Gaschen, A.; Ricka, J.; Geiser, M. *Environ. Sci. Technol.* **2008**, *42*, 5667-5674.

B. Evaluation of Basic Toxicity of Various Metal Nanoparticles for QSAR Modeling

Studies conducted by Nicole Schaeublin, MS in collaboration with Jerzy Leszczynski, PhD

Quantitative Structure Activity Relationship (QSAR) methods are based on the assumption that the variance in a given physico-chemical or biological (e.g., toxicity) property in a set of compounds (so-called endpoint) was determined by the variance in their molecular structures, encoded by so-called descriptors. This was particularly important in relation to the ethical issues, costs and the expected increase in number of engineered NMs that will be utilized in the future. The QSAR method can be used to predict the toxicity of various metal nanoparticles by using molecular descriptors along with results from standard toxicity evaluations. However, in order to validate the model, the mathematical equation requires data from many different nanoparticles.

The first step of this study involves predictions of physicochemical properties of the studied NMs, in order to develop a set of the descriptors to be used to study their toxicity. For the initial investigations five compounds- nickel oxide, silicon dioxide, tin oxide and titanium dioxide- were selected from the group of metal oxides tested experimentally. Based on the experimental crystal lattice parameters we constructed and studied metal (semimetal) oxides (MeOx) molecular clusters. For all these compounds geometric optimizations were done.

Various size clusters were considered, i.e., metal oxide clusters of size range from 2 to 500 atoms. In order to obtain cubic clusters having an appropriate size, the lattice parameters were subsequently increased in respect to all three dimensions. At first, we increased twice one of the dimensions of the initial unit cell. Thereafter, we used the initial cluster structure obtained in the previous step and additionally increased twice the second dimension. Then, we doubled the third of the unit cell dimensions, increasing the cluster size more than twice the initial size. We repeated this procedure until we obtain clusters with the proper size. The results are presented in Table 4, where the saturation point refers the size of the considered metal oxide nano-cluster (in Å) at which the electronic property value (Band GAP energy) of that cluster converges to the value of bulk size metal oxide. The Band GAP energy generally refers to the energy difference (in electron volts) between the top of the valence band and the bottom of the conduction band (for example, in insulators and semiconductors).

Having both, high-quality experimental data and molecular descriptors: (i) image descriptors (based on images taken from transmission electron microscopy) and (ii) quantum-mechanical descriptors (based on quantum-chemical calculations), a computational study was carried out. The first step of this study was aimed at investigating how the method of splitting data into a training set and a test set influences the external predictivity of quantitative structure–activity relationships (nano-QSAR) models.

Table 4. Experimental Compounds Selected From the Group of Metal Oxides Based On Their Experimental Crystal Lattice Parameters

Metal / Semi-Metal Oxide	Saturation point [Å]	Number of atoms	Total energy [eV]	Band GAP energy [eV]
Al ₂ O ₃	12	160	-31466	-4.59
ZnO	11	144	-23157	-3.87
SnO ₂	13	144	-41962	-3.85
SiO ₂	10	96	-21060	-3.23
TiO ₂	13	144	-31518	-7.47

For the initial computational investigations five alternative splitting algorithms were selected, namely (i) a commonly used algorithm ('X:1'), in which the compounds were sorted according to the ascending response values, y , and every x th (e.g. third) was selected into the test set; (ii–iv) three variations of the Kennard–Stone algorithm [9] and (v) the duplex algorithm [10]. In the next step, the experimental data and molecular descriptors were used to calibrate and validate the nano-QSAR models according to the golden standards established by the Organization for Economic Co-operation and Development (OECD) [11]. We employed a wide range of different regression techniques, such as Multiple Linear Regression (MLR), Ordinary Least Squares (OLS), Partial Least Squares (PLS), and Principal Component Regression (PCR). In order to select the optimal combination of the molecular descriptors to be utilized in the final nano-QSAR model, we employed the Holland's genetic algorithm. The algorithm minimizes the prediction error by searching for the most optimal combination of the descriptors.

Individual nano-QSAR models were characterized by low values of the statistics: goodness-of-fit ($0.51 < R^2 < 0.65$) and external predictivity ($0.34 < Q^2_{Ext} < 0.53$). The absolute values of root mean square error of prediction (RMSEP) were ranged from 0.45 to 0.58 logarithmic units of LD50. The descriptors-to-compounds ratio (5:1) was satisfactory. Various statistical parameters for ten models are presented in the Table 5.

Table 5. Statistical results for Individual nano-QSAR models

Model	I	II	III	IV	V	VI	VII	VIII	IX	X
R^2	0.67	0.52	0.49	0.61	0.59	0.52	0.53	0.61	0.59	0.52
Q^2_{Ext}	0.53	0.41	0.42	0.49	0.51	0.41	0.48	0.48	0.34	0.41
R^2	0.51	0.57	0.51	0.53	0.56	0.55	0.52	0.55	0.51	0.65
RMSE _C	0.21	0.27	0.38	0.34	0.33	0.39	0.31	0.34	0.43	0.29
RMSE _{CV}	0.44	0.48	0.52	0.41	0.59	0.47	0.46	0.37	0.49	0.47
RMSE _P	0.49	0.56	0.54	0.58	0.45	0.52	0.49	0.58	0.55	0.52

Particle size is not the only possible factor influencing toxicity of engineered NMs. The following features should be also considered: size distribution, agglomeration state,

shape, porosity, surface area, chemical composition, structure-dependent electronic configuration, surface chemistry, surface charge, and crystal structure. Thus, novel “nano-descriptors” should reflect these characteristics. In order to find the best structural parameters reflecting the essential properties of the studied NMs, we proposed a set of image descriptors (based on images taken from TEM) and quantum-mechanical descriptors (based on quantum-chemical calculations).

Based on the experimental crystal lattice parameters, we constructed metal (semimetal) oxides molecular clusters with the XP molecular modeling software package. We utilized those structures as inputs for quantum–mechanical calculations which included two stages: (i) optimization of the molecular geometry with respect to the energy gradient and (ii) calculation of the descriptors based on the optimized geometry. The calculations were performed at the semi-empirical level of the theory with use of PM6 method in the MOPAC 2009 software package. We calculated 25 molecular descriptors (Table 6).

Table 6. Definition of quantum-mechanical descriptors

Symbol	Definition of quantum-mechanical descriptors
HOF	Standard heat of formation of metal oxide nanocluster
Hof_k	Standard heat of formation of cation
U	Lattice energy
TE	Total energy
EE	Electronic energy
Core	Core–core repulsion energy
SAS	Solvent accessible surface
HOMO	Energy of the Highest Occupied Molecular Orbital
LUMO	Energy of the Lowest Unoccupied Molecular Orbital
GAP	HOMO-LUMO energy gap
η	Chemical hardness
S	Total softness
ω	Electrophilicity index
μ	Electronic chemical potential
EV	Valance band
EC	Conduction band
Q-	Lowest negative Mulliken’s partial charge on the molecule
Q+	Highest positive partial charge on the molecule
Ahof	Polarizability derived from the heat of formation
Ad	Polarizability derived from the dipole moment
EN	Mulliken’s electronegativity
Hard	Parr and Pople’s absolute hardness
Shift	Schuurmann MO shift alpha
HOF _c	Standard heat of formation in a solution represented by the Conductor-like Screening Model (COSMO)
TE _c	Total energy in a solution represented by the Conductor-like Screening Model (COMSO)

Moreover, based on the TEM microscopic images, we have converted the TEM pictures to a numerical matrix in which each numerical value corresponds to a single pixel of the original picture and calculated a set of image descriptors reflecting the size distribution, agglomeration state, shape, porosity, and surface area for all studied nanometer–sized metal and semimetal oxides. We calculated the 12 image descriptors listed in Table 7.

Table 7. Definition of Size Descriptors

Symbol	Definition of size descriptors
A	Area
V	Volume
dS	Surface diameter
dV/m	Volume/mass diameter
dSauter	Volume/surface diameter
AR_x	Aspect ratio X
AR_y	Aspect ratio Y
PX	Porosity X
PY	Porosity Y
P	Total porosity
Ψ	Sphericity
fcirc	Circularity

Having high-quality experimental data and molecular descriptors that included (i) image descriptors (based on images taken from transmission electron microscopy) and (ii) quantum-mechanical descriptors (based on quantum-chemical calculations), we developed a QSAR model following the golden standards and recommendations of the Organization for Economic Cooperation and Development (OECD) [11]. We employed the Multiple Linear Regression (MLR) as the chemometric method of modeling. In order to select the optimal combination of the molecular descriptors to be utilized in the final QSAR model, we employed the Holland's genetic algorithm (GA) [12]. The algorithm minimizes the prediction error by searching for the most optimal combination of the descriptors. Genetic Algorithm-Multiple Linear Regression calculations were performed with MATLAB 7.6 and PLS Toolbox 5.2.

We obtained a QSAR equation utilizing only two descriptors to successfully predict the cytotoxicity of the MeOx nanoparticles.

$$\log(1/EC50)^{[13]} = 2.442 + 0.192*HoF + 0.429*EN$$

Table 8. Results from QSAR Model.

ID	Heat of formation [HoF]	Mulliken electronegativity [EN]	Observed log (1/LD50) [molar]	S (3:1)	Predicted log(1/LD50) [molar]	Leverages	Residuals
ZnO	-449.38	8.329	3.32	1	3.28	0.437	0.04
In ₂ O ₃	-52.07	6.784	2.92	1	3.01	0.278	-0.09
La ₂ O ₃	-157.72	6.455	2.87	2	2.88	0.196	-0.01
CoO	-1675.45	8.251	2.83	1	2.85	0.497	-0.02
SnO ₂	-145.79	4.685	2.67	1	2.43	0.095	0.24
Mn ₂ O ₃	-89.59	4.998	2.64	1	2.53	0.107	0.11
WO ₃	-728.13	6.728	2.56	2	2.77	0.143	-0.21
Bi ₂ O ₃	-148.46	5.343	2.50	1	2.60	0.107	-0.10
NiO	68.02	4.472	2.49	1	2.44	0.136	0.05
Gd ₂ O ₃	-1784.98	5.909	2.41	1	2.20	0.508	0.21
Sb ₂ O ₃	-206.73	4.459	2.31	2	2.35	0.091	-0.04
Cr ₂ O ₃	-235.25	4.356	2.30	1	2.31	0.092	-0.01
V ₂ O ₃	-139.54	3.239	2.24	1	2.05	0.175	0.19
Y ₂ O ₃	-135.28	3.348	2.21	1	2.08	0.164	0.13
SiO ₂	-618.26	3.813	2.12	2	2.04	0.162	0.08
Fe ₂ O ₃	-416.51	4.573	2.05	1	2.31	0.081	-0.26
Al ₂ O ₃	-599.96	3.436	1.85	1	1.95	0.204	-0.10
TiO ₂	-651.58	4.334	1.76	1	2.17	0.120	-0.41

The descriptor HoF represents the density of the MeOx nanoparticles surface and the availability of the metal cations. In other words, HoF descriptor was related to how much energy should be delivered to detach the metal and transform an atom into its fully ionized form. The consequence is to initiate changes in cell viability, generation of reactive oxygen species (ROS) and the response of human keratinocyte (HaCaT) cells. The second descriptor, EN, was closely related to the redox potential of the studied structures. Those oxides having high EN usually exhibit the strong reductive properties (easily detach the electron), which enhances their cytotoxicity to the HaCaT cell-line.

An integral part of QSAR modeling was to appropriately describe the borders of the optimum prediction space of the model. We verified the applicability domain by using the Williams plot, which was the plot of the leverage values *versus* cross-validated standardized residuals (Figure 18).

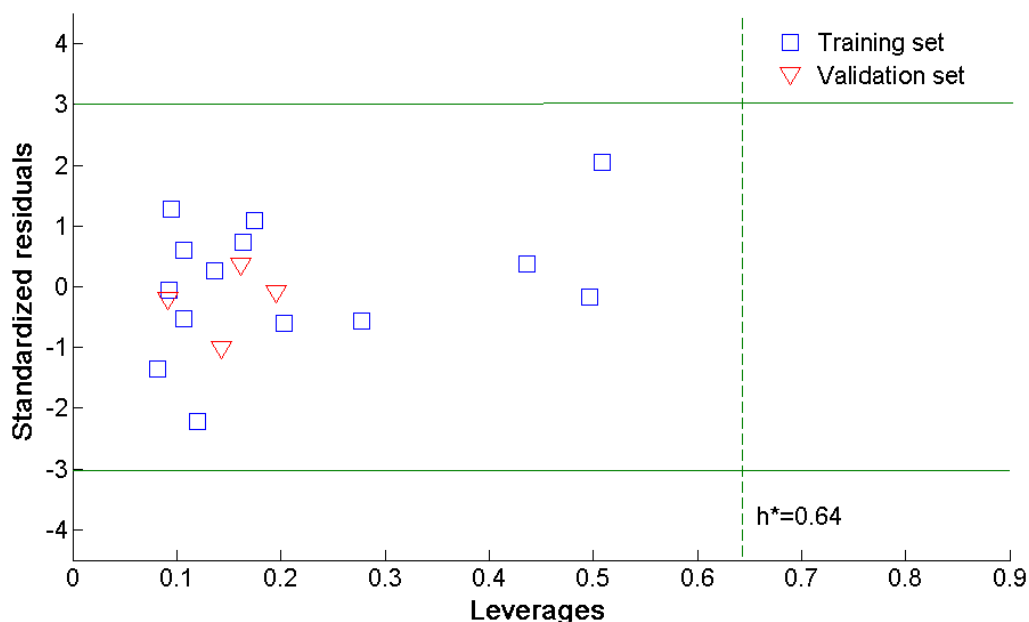


Figure 18. Williams plot describing applicability domains of GA-MLR model. Solid lines represent the residual threshold (0 ± 3 standard deviation units), and dotted line represents the critical leverage value (h^*).

The QSAR model was characterized by satisfactory goodness-of-fit, robustness and external predictive performance (the statistical measures are summarized in Table 9).

Table 9. Statistical Measures for QSAR Model.

Feature	Measure	nanoQSAR model
Goodness-of-fit	R2	0.82
	RMSEC	0.175
Robustness	Q2CV	0.70
	RMSECV	0.222
Predictivity	Q2Ext	0.84
	RMSEP	0.112

A visual correlation between the experimental and predicted values of $\log(1/EC50)$ is presented in Figure 19.

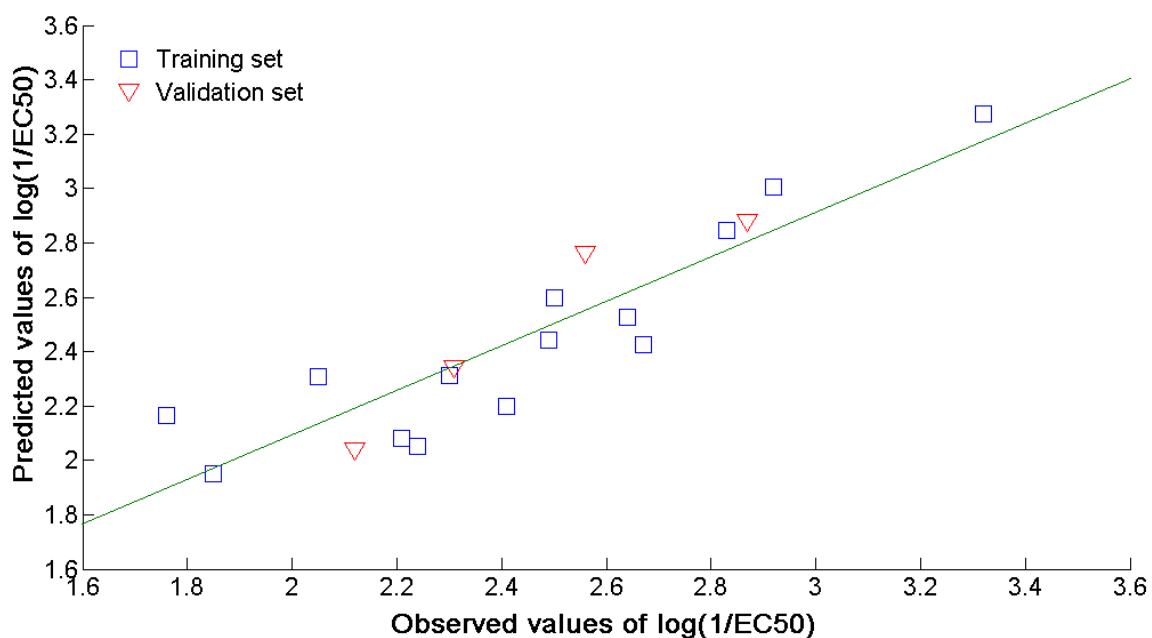


Figure 19. A visual correlation between the experimental and predicted values of $\log(1/EC_{50})$

This project was presented during a poster session at the Society of Toxicology meeting in San Francisco on 13 March 2012. The poster is shown on the next page (Figure 20).



Application of QSAR Modeling to Predict Metal Nanoparticle Toxicity

Nicole M Schaublin¹, Elizabeth I Maurer¹, Agnieszka Gajewicz², Jerzy Leszczynski³, and Saber M Hussain¹

¹Molecular Bioeffects Branch, Human Effectiveness Directorate, Air Force Research Laboratory, Wright-Patterson AFB, OH,

²University of Gdansk, Faculty of Chemistry ul Sobieskiego 18 80-952 Gdansk, Poland, ³Jackson State University, MS



Objective

The goal of this study was to develop a computational model to predict metal oxide nanoparticle (MeONP) toxicity in eukaryotic cells using data obtained from dermal exposure.

Introduction

Due to the increase in NP applications, there is a need to quickly screen their potential toxicity. However, as traditional toxicity evaluations are costly and time consuming, computational methods are being used as cost effective options to identify potential toxic NPs. The present study demonstrated that the quantitative structure-activity relationship (QSAR) method can be used to predict the toxicity of an assortment of MeONPs based on the results of standard toxicity evaluations. TEM images of the NPs alone and in the cells were used to define several molecular descriptors for over-one different metal oxides. Additionally changes in cell viability were evaluated using a human keratinocyte (HaCaT) cell line as a model for dermal exposure. The results of the toxicity assays identified a LD₅₀ value for all the NPs and indicated that zinc oxide (ZnO) had the most toxic of the MeONPs tested. The ZnO LD₅₀ value was 20 µg/ml while the majority of the other NPs, including indium, lanthanum, and titanium, had a LD₅₀ > 200 µg/ml. The combined experimental-theoretical study allowed for the development of a model that links experimental data with descriptors acquired based on the computationally predicted molecular characteristics. Such a model could be applied not only to metal oxides investigated in the current work, but also to unexplored related species. This approach provides an efficient method of evaluation of various groups of nanoparticles.

Experimental Methods

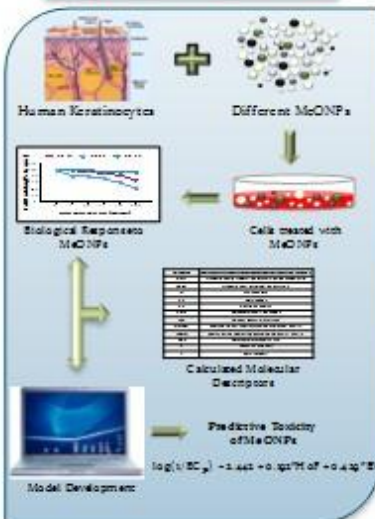


Figure 1. Experimental methods. Air Force Research Laboratory.

Metal Oxide Nanoparticle Characterization

Table 1. Average Diameter of MeONPs Before and After Dispersion in Media. All of the MeONPs agglomerated when dispersed in media.

Metal Oxide Nanoparticles	NP Symbol	Average Particle Size (nm)	Average Particle Size in media (nm)	Zeta Potential (mV)
Aluminum oxide	Al ₂ O ₃	55	3752 ± 17.8	-20.2 ± 2.2
Antimony III oxide	Sb ₂ O ₃	205.0	205.0 ± 11.0	-19.2 ± 0.2
Bismuth III oxide	Bi ₂ O ₃	35	202 ± 10.7	-21.2 ± 1.2
Cadmium II oxide	CdO	<100	127 ± 11.9	-2.4 ± 1.1
Cerium III oxide	Ce ₂ O ₃	20	227 ± 3.2	-1.2 ± 10.1
Chromium III oxide	Cr ₂ O ₃	20	210.2 ± 11.2	2.7 ± 2.0
Chromium oxide	Cr ₂ O ₃	40-60	270.2 ± 126.0	10.2 ± 2
Copper II oxide	CuO	23	272.0 ± 6.0	-19.1 ± 1.2
Chromium oxide	Cr ₂ O ₃	<100	217.2 ± 11.2	21.2 ± 1.2
Indium III oxide	In ₂ O ₃	20.2	224.2 ± 20.1	-19.2 ± 1.2
Lanthanum III oxide	La ₂ O ₃	12.0	212.2 ± 10.1	-12.2 ± 1.2
Manganese oxide	Mn ₂ O ₃	20.2	211.2 ± 7.2	-1.2 ± 1.2
Nickel II oxide	NiO	20	222.2 ± 2.2	-12.1 ± 1.1
Silver chloride	AgCl	12	202 ± 20.2	-1.1 ± 1.0
Ti IV oxide	TiO ₂	12.2	227.2 ± 12.2	-19.2 ± 1.2
Titanium IV oxide	TiO ₂	20	202 ± 20.2	-1.1 ± 1.0
Tungsten VI oxide	WO ₃	20-20	170.2 ± 2.2	-1.1 ± 2.0
Vanadium III oxide	V ₂ O ₃	20.2	122.2 ± 10.1	-12.2 ± 1.2
Zinc oxide	ZnO	20	222.2 ± 2.2	-12.1 ± 1.2
Zincum II chloride	ZnCl ₂	10-7	20.2 ± 10.2	-1.2 ± 1.1

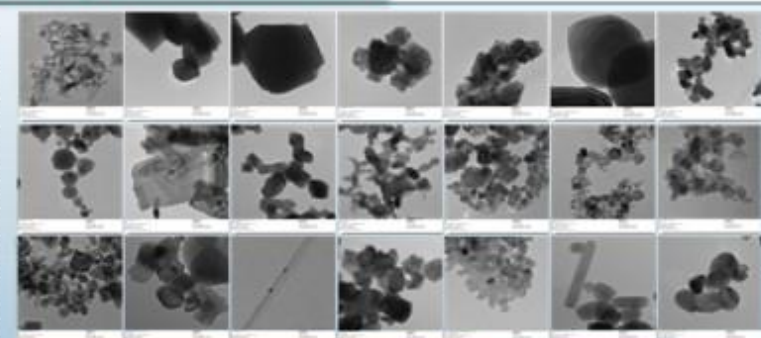


Figure 2. Transmission Electron Microscopy Images of the MeONPs.

Experimental Results

Cellular Viability

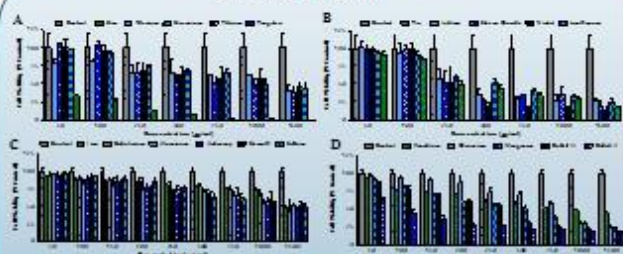


Figure 3. Cellular Viability Assays. Relative cell viability of Human Keratinocytes after exposure to 21 MeONPs. All of the MeONPs were toxic to the keratinocytes, however some of the particles had no observed cell viability reduction at the tested concentrations.

Summary

- Human keratinocytes were used as a model for dermal toxicity exposure to 21 different MeONPs.
- The LD₅₀ and molecular descriptors were calculated for each particle from the cell viability assay.
- The LD₅₀ and molecular descriptors were used to successfully develop a nanoQSAR model to accurately predict the toxicity of MeONPs.

Acknowledgements

This project is funded through the Air Force Office of the Surgeon General. Ms. Schaublin and Ms. Maurer are funded through the Henry M. Jackson Foundation.

Theoretical Model

nanoQSAR Model

$$\log(1/EC_{50}) = 2.442 + 0.192 * HoF + 0.429 * EN$$

$R^2 = 0.82$ $Q^2_{LO} = 0.70$ $Q^2_{RO} = 0.84$
 $RMSE_{LO} = 0.175$ $RMSE_{LO} = 0.222$ $RMSE_{RO} = 0.212$

Table 2. Mechanical Descriptors Used to Calculate nanoQSAR model

Symbol	Definition of Quantum Mechanical Descriptors
HoF	Standard heat of formation of metal oxide nanocluster
EN	Mulliken's electronegativity

Model Validation

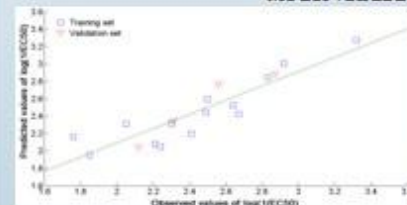


Figure 4. Plot of experimentally determined versus predicted log values of 1/EC₅₀. The straight line represents perfect agreement between experimental and calculated values. Squares represent values predicted for the metal oxides from the training set; triangles represent data calculated for metal oxides from the validation set. The distance of each symbol from the green line corresponds to its deviation from the related experimental value.

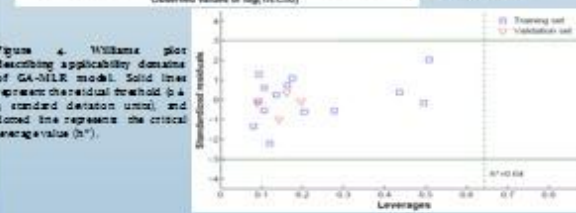


Figure 5. Williams plot describing applicability domains of GA-BMLR model. Solid lines represent the residual threshold 0.5 standard deviation interval, and dotted line represents the critical leverage value (h*).

Figure 20. Poster presented at the SOT conference on 13 March 2012

Additional data were generated to make the model more reliable, including the LSC (least significant concentration of particles that induce ROS) and LD₂₀₀ (lowest dose that generates 50% more ROS than the control). Therefore, all 21 metal oxide nanoparticles (MeONPs) were assessed to see if they generate reactive oxygen species (ROS). Each MeONP was tested at 3 different concentrations based on the LD₅₀ values calculated from the viability assay in order to streamline the process. However, because previous results failed to show a significant increase in ROS after 24h, the cells were exposed to the MeONPs for 4h. We shortened the time-point because ROS is a fairly early cellular response and the cells' antioxidant defenses may have already eliminated any ROS generated before measured at 24h. The results from the 4h exposure demonstrated significant amounts of ROS after exposure to all MeONPs, suggesting that the cell was scavenging the ROS produced and ameliorating the toxicity of the NPs (Figure 21). Further experiments must be conducted to calculate the LD₂₀₀ and LSC.

References

- [9] Kennard, R.W.; Stone, L.A. *Technometrics* **1969**, *11*.
- [10] Snee, R.D. *Technometrics* **1977**, *19*, (4), 415-428.
- [11] Guidance Document on the Validation of (Quantitative) Structure Activity Relationship [(Q)SAR] Models, Organization of Economic Cooperation and Development, can be found under <http://www.oecd.org>, **2007**.
- [12] Goldberg, D.E.; Holland, J.H. *Machine Learning* **1988**, *3*, 95-99.
- [13] Puzyn, T.; *et.al.* *Nature Nanotechnology* **2011**, *6*, 175–178.

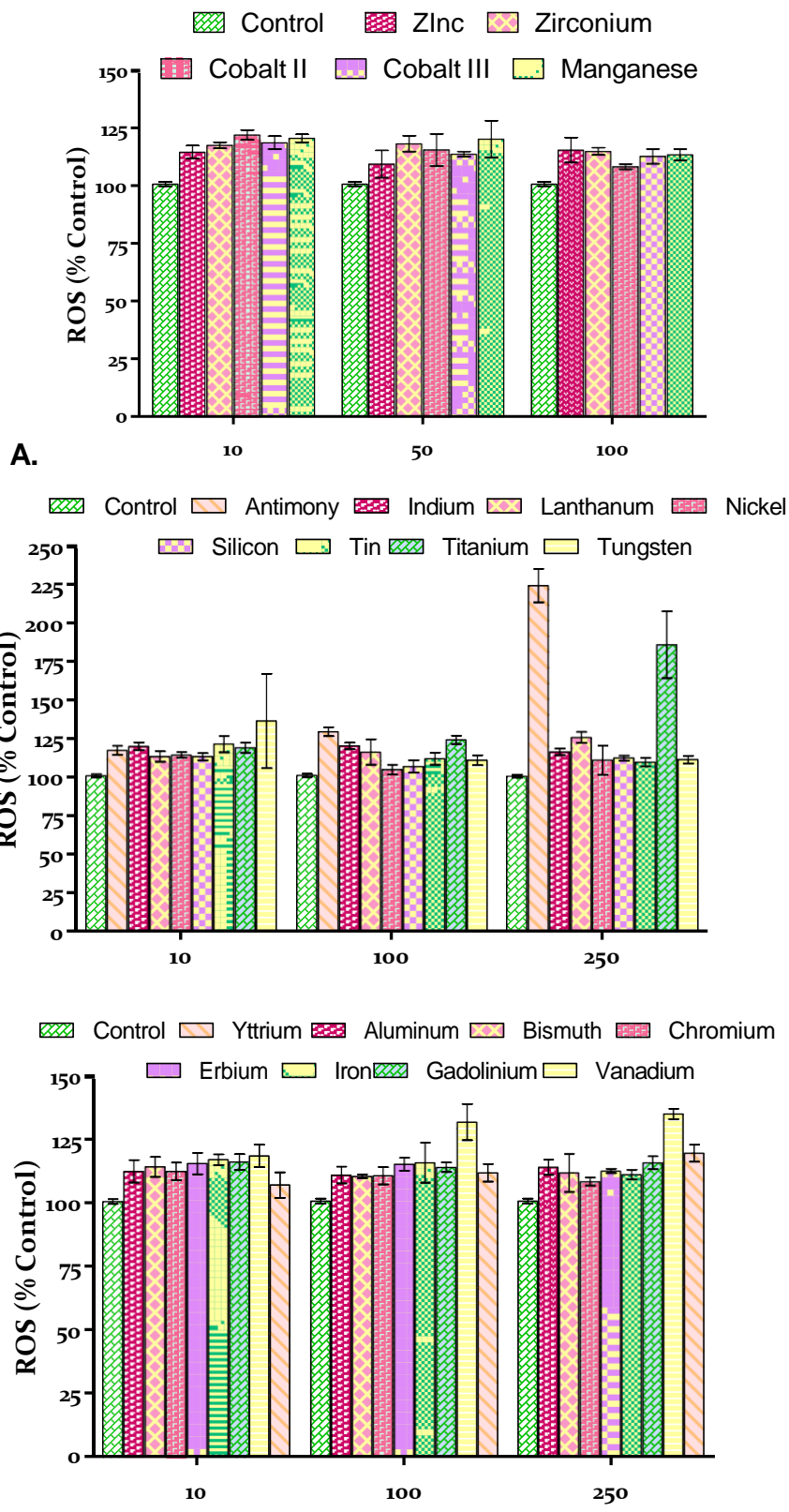


Figure 21. Generation of ROS after 4h exposure to MeONPs. There was a significant increase in ROS after exposure to all NPs.

C. Fundamental Understanding of Biological Compatibility of Nanomaterials

Studies conducted by Ravindra Pandey, PhD

In the first study, the interaction of protein with nanoparticle was investigated *via* examining the interaction of tryptophan (Trp) with gold (Au) nanoparticles. The results showed that the interaction strength is site-selective and is dominated by π interactions together with small ionic interactions. In the Trp–Au bio-conjugated complex, the nature of Trp's molecular orbitals is modified by the hybrid states associated with Au as low lying excited states. The non-radiative energy transfer to these states appeared to cause the experimentally observed fluorescence quenching Trp interacting with gold.

For the second study, we performed a simulation of lipid bilayers using first principles methods. The calculated results showed, for the first time, the accuracy and reliability of such methods in calculating the structural properties for DMTAP, DMPC and DMPE bilayer systems. We also examined the solvation effects, and find that the presence of the water molecules is essential in stabilizing the configuration of the DMPE bilayer. It also facilitated a significantly large change in its dipole moment along the γ direction. The results therefore predicted a relatively high activity of the hydrated lipid layer of DMPE relative to that of DMPC for nanoparticles.

1. Protein-Nanoparticle Interactions: Tryptophan with Gold

(J. Physical Chemistry C 115, 22818 (2011))

Introduction

The miniaturization of structures in the guise of nanoscale materials have created a so-called nanoplatform for applied biomedical research in developing novel and improved diagnostics and therapeutics [14]. Nanoparticles possess large surface areas for biomolecular reactions, thus providing a promising pathway for combining biomolecular functionality with unique electronic and optical attributes to create hybrid nano scaffolds. Such scaffolds with specific features are of particular interest in recognition and modulation of biomacromolecules, protein interactions, protein-nucleic acid interactions, enzyme activity, and biomimetic reactions [14–16]. Due to intriguing optoelectronic properties and biocompatibility, gold nanoparticles have been widely exploited for diagnostics and therapeutic applications [15]. The long term fascination with gold was substantially facilitated by the ease of their size-controlled synthesis and functionalization with multifunctional ligands such as amino acids, proteins, peptides and DNA [15]. Serum proteins associate with the nanoparticles in biological medium to form a protein 'corona' which defines the biological identity of the particles within the biological system, thus making the protein–nanoparticles interaction of particular interest [17]. The adsorption of proteins on nanoparticles can alter their three dimensional structure, activity and biological responses, leading to unpredicted perturbations in the system.

The protein-nanoparticle interactions and their effects on proteins structure and activity are generally determined by various spectroscopic and thermodynamic methods. One method, intrinsic fluorescence quenching is a powerful spectroscopic tool for

investigating protein structure and binding interactions with nanoparticles [18–19]. The fluorescence of protein is due to aromatic amino acid residues, among which, tryptophan (Trp) has a strong fluorescence and high quantum yield attributed to its π - π^* transitions of *indole* functional group [20–21]. Trp is an essential amino acid in the human-diet and is known to form hydrogen bonds together with weak ionic bonds in a conjugated system. Also, the *indole* group contains a benzene ring fused with nitrogen containing a pyrrole ring, resulting in a delocalized π electron cloud. At the excitation wavelength of 280 nm, the fluorescence of protein is dominated by Trp along with minor contribution from tyrosine and phenylalanine. The intensity and wavelength of Trp fluorescence are sensitive to the environment, and hence indicative of the protein conformational alterations upon binding to nanoparticles.

Earlier studies suggested that gold efficiently quenches the fluorescence of Trp9 and the efficiency of the quenching represents the binding affinity and accessibility of gold particles to the Trp residue in protein. In the experimental study of bioconjugated gold nanoparticles with BSA protein, quenching of the static mode of intrinsic Trp fluorescence revealed the formation of the ground state complex consisting of protein and nanoparticles [18,23-24]. The moderate binding observed for gold-BSA conjugation was consistent with weak van-der Waals and hydrophobic interactions between nanoparticle and biomolecules [18,23–24].

We next investigated the Trp fluorescence quenching by gold nanoparticles using quantum mechanical methods. We employed first-principles methods based on density functional theory (DFT) to determine the details of the interaction between gold (Au) nanoparticles and amino acid tryptophan (Trp). We determined the (i) preferred interaction site of Trp, (ii) chemical bonding of Au-Trp bioconjugates and (iii) modifications in Trp's electronic states that may be responsible for its fluorescence quenching in the bioconjugate configuration.

Au₃₂, a cage-like, hollow, gold cluster, 8.9 Å in diameter was used to represent gold nanoparticles. A recent report on magic numbers in gold clusters by using the shell from the Jellium model suggest that Au₃₂ is highly stable and a good potential candidate for studying cage-like structures with an energy gap comparable to other cage-like structures: C₆₀, Au₁₆, Au₄₂ [25]. The binding sites offered by Trp are salt-bridge interaction involving the carboxylic group (–COO⁻), charge-solvent interaction involving the *indole* ring, and amine group interaction involving –NH₂ group [26]. The equilibrium configurations with corresponding interaction energies, density of states, molecular orbitals, and charge density distribution of the Trp–Au₃₂ complex were obtained through DFT-based quantum mechanical calculations; all of which help define the interactions between Au and Trp.

Computational Method

All calculations were carried out within the framework of density functional theory (DFT) as implemented in SIESTA code using exchange-correlation function proposed by Perdew, Burke and Ernzerhof (PBE) [27-28]. Only the valence electrons of each

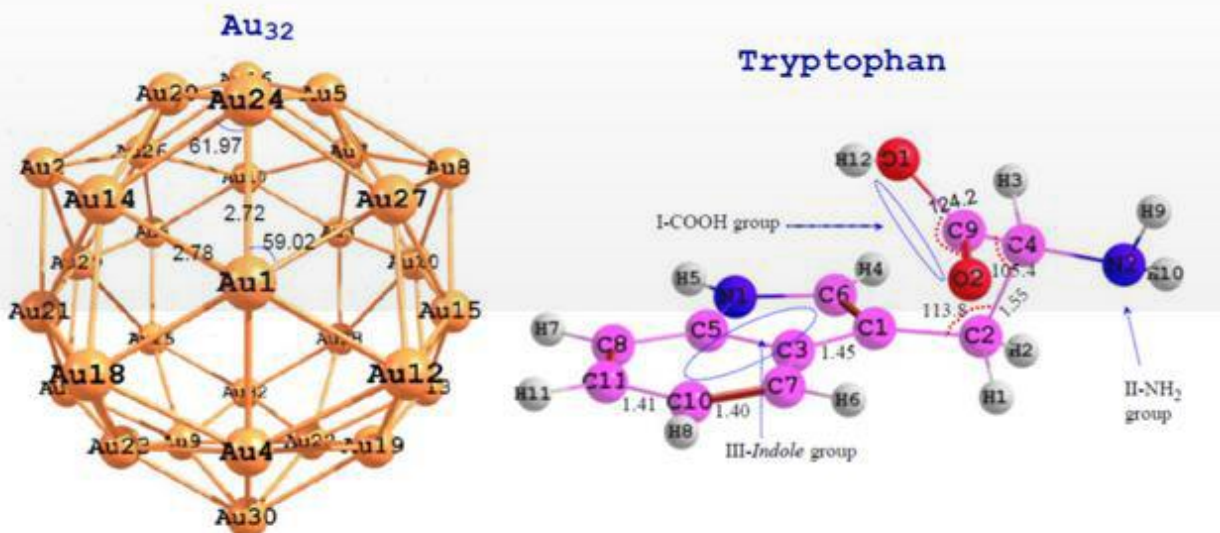
chemical species in the Trp and Au nanocluster were treated explicitly and their interactions with ionic cores were described by ultra-soft norm-conserving pseudopotentials using the Trouiller and Martins scheme [29]. The valence configurations of H ($1s^1$), C ($2s^2 2p^2$), N ($2s^2 2p^3$), O ($2s^2 2p^4$), and Au ($5d^{10} 6s^1$) were represented by double-zeta basis sets with polarization functions (DZP) [30]. The numerical integrals were performed on a real space grid with an equivalent energy cutoff of 3400 eV. The calculations were considered to be converged when the force on each ion was less than 0.001 eV/Å. Also, total energy convergence criterion of 10^{-5} eV was used.

Results and Discussion

The 32 atom cluster of Au was found to favor a cage-like structure [31]. The calculated ground state configuration of Au_{32} has icosahedral I_h symmetry with hollow shape of the cluster as shown in Figure 22a. The geometry was obtained by placing one atom on each pentagon of a dodecahedron. The cluster evidenced only two different kinds of sites on the cage: 12 sites with a coordination number five and 20 sites with a coordination number six; i.e. each atom binds to either five or six neighboring gold atoms. The symmetry is similar to the truncated icosahedron C_{60} , with interchanged vertices and planes. Therefore, two bond lengths of 2.72 and 2.8 Å were obtained for the five-coordinated sites and six-coordinated sites, respectively (Figure 22a). The total charge density of Au_{32} is also shown in Figure 22b. The calculated structural properties of Au_{32} are in good agreement with the previously reported values using density functional theory [31]. The gap between the highest occupied molecular orbital (HOMO) and the lowest unoccupied molecular orbital (LUMO) is calculated to be 1.31 eV.

The presence of an *indole* functional group together with an amine and a carboxyl functional groups is the discriminating structural characteristic of the aromatic amino acid residue tryptophan (Trp). Figure 22 shows the optimized ground state configuration and total charge density of Trp molecule. The *indole* ring is oriented perpendicular to the carboxyl and amine groups. In the optimized configuration, the *indole* ring is 113.77° out-of-plane with respect to the plane containing $-COOH$ and $-NH_2$ functional groups i.e. C1-C2-C4. The C-C and C=C bond lengths in the hexagonal benzene ring of *indole* are 1.42 and 1.40 Å, respectively. The C-C and C=C bond lengths of the pentagonal pyrrole ring of *indole* are 1.45 and 1.39 Å, respectively. The C-C bond distinguishing the plane of the *indole* ring and the $-COOH/-NH_2$ functional groups is 1.56 Å making an angle (C2-C4-C9) of 105.45° with $-COOH$ group directed towards the *indole* ring. The O-C-O angle of $-COOH$ group is 123.23° . The calculated HOMO-LUMO gap and dipole moments are 3.66 eV and 4.01 debye (D), respectively. The calculated values of bond lengths and bond angles of Trp are in excellent agreement with the previously reported values also obtained using DFT calculations [32].

(a) Ground state configurations



(b) Total charge density

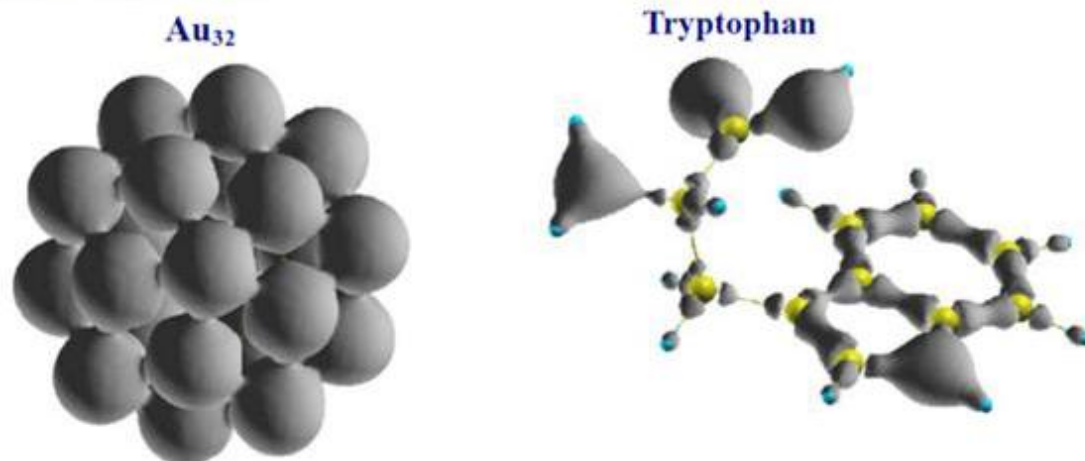


Figure 22. The calculated ground state configurations and total charge density of (a) (Au_{32}), and (b) Trp. The Au_{32} interaction sites for tryptophan are also shown. The charge density is shown at 1/3rd of its maximum isosurface value.

The optimized isomeric configurations of Trp- Au_{32} conjugates involving (i) -COOH (ii) -indole, and (iii) -NH₂ functional groups as preferred interaction sites are presented in Figure 23. No geometrical constraints were imposed to obtain the optimal structures of these isomeric configurations of Trp- Au_{32} . The binding energy, bond-lengths, dipole moment and HOMO-LUMO energy gap of the optimized isomeric configurations are listed in Table 10.

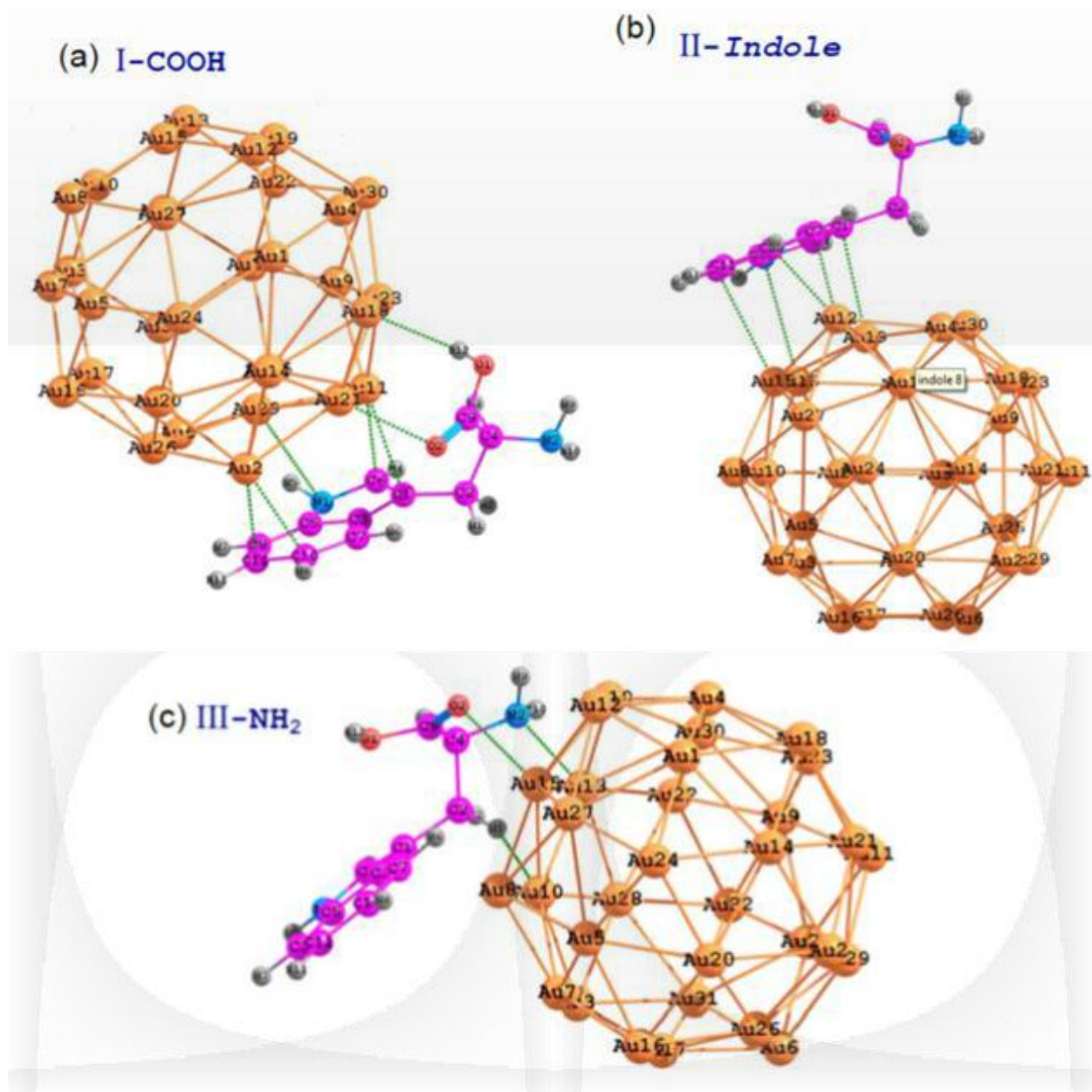


Figure 23. The ground state configurations of Trp-Au₃₂ complex.

Table 10. The calculated structural and electronic properties of the isomeric configurations of the Trp–Au₃₂ complex.

Isomers	I–COOH group	II– <i>Indole</i>	III–NH ₂
Binding energy/eV	-2.72	-1.86	-1.8
R _(Cluster-Trp)	-	-	-
Au – N	3.0	3.31	2.60
Au – O	2.58	-	2.9
Au – C <i>indole</i> -benzene	2.48	2.35	-
Au – C <i>indole</i> -pyrrole	2.38	2.95	-
Au – H	2.57	2.71	2.40
Dipole moment/D	5.97	3.78	7.44
HOMO–LUMO gap/eV	1.2	1.51	1.45
Mulliken charge/e \bar{e}	Au = -0.062 Trp = +0.062	Au = -0.08 Trp = +0.08	Au = -0.13 Trp = +0.13

The binding energy of the Trp–Au₃₂ cluster complex is calculated as the difference of the energy associated with the equilibrium configuration and the energies associated with the isolated cluster and Trp. As noted from Table 10, the salt bridge structure involving the –COOH group appears to be energetically more favorable than the two comparably interacting –*indole* and –NH₂ groups. The larger binding energy of Trp–Au₃₂ in –COOH group conjugation appears to result from the interaction of Au with carbonyl oxygen atoms (Figure 23a). Besides the O_{Trp}–Au interaction, there exists a weak non-conventional O_{Trp}–H···Au interaction, which seems to provide additional stability to the Trp–Au complex. Figure 23a also shows Au atoms interacting with *indonyl* functional groups, including both of its pyrrole and benzene rings in Trp. There are some structural changes observed for Trp. The angle C1–C2–C4 is found to be 117° compare to the initial value of 113.77° and the angle C2–C4–C9 becomes 111.9° compare to its initial value of 105.45°. However, none of the H_{Trp} is found to be perturbed. With regards to the –*indole* group interaction, Au atoms are found to be well interacting with *indole* group of Trp (Figure 2b). However, no noticeable structural changes occurred from *indole* group interaction. The angles C1–C2–C4 and C2–C4–C9 show minor alterations and are found to be at 114.54° and 106.93° respectively. Unlike the –COOH site interaction having an –*indole* contribution, the –NH₂ site interacts with the nitrogen of the amine, oxygen of the carboxyl group and hydrogen of the carbon backbone (Figure 23c). Figure 2c shows the double coordination of Au with –COOH and –NH₂ groups and the angles C1–C2–C4 and C2–C4–C9 appear at 118.76° and 112.69° respectively. Additionally, the angle between the –COOH group and –NH₂ group in Trp was reduced to 106.33° from its initial value of 109.52°.

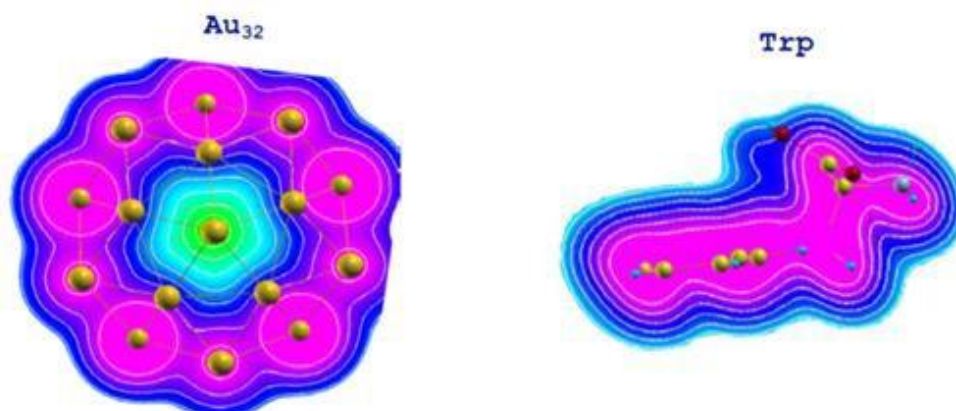
In protein chemistry, structures involving the –COO– group of an amino acid are known as salt bridge structures, whereas interactions involving the –*indole* ring are represented in charge solvent structures [33]. Following this nomenclature, the Trp–Au₃₂ isomer

formed through the -COOH group interaction can be classified as a salt bridge structure but as noted from Figure 23a and Table 10, the Au cluster is equally interacting with the *-indole* group-. Hence, the isomeric configuration involving the -COOH group may be considered to have characteristics of both a salt bridge as well as a charge solvation structure, showing maximum binding energy (Table 10). Likewise, the isomeric configuration involving the *-indole* group may be considered as a charge solvation structure. The -NH_2 group isomer shows double coordination with the -COOH and -NH_2 groups (Figure 23c). Thus, the calculated results predict the ground state complex, which is in agreement with the experimental observation with a preference for a mixed salt bridge and a charge solvation type bonding interaction [23,24].

The Mulliken charge analysis of the isomeric configurations of the Trp-Au₃₂ complex reveals a small charge transfer during conjugation and is noted in the Trp to Au cluster at all three sites of interaction. The results therefore excluded a charge transfer as the main mechanism for the Trp-Au₃₂ conjugation for the -COOH and *-indole* group interaction. However, the charge transfer is comparatively higher in the case of the -NH_2 group interaction that may govern the conjugation. This is in agreement with the relatively larger dipole moment of 7.44 debye (D) for this complex during the -NH_2 group interaction compared to the native Trp, suggesting the rearrangement of the electron density when the complex forms. The comparatively large dipole moment of the -COOH group compared to that of the *-indole* group is co-related with a larger structural rearrangement evidenced during the formation of -COOH group conjugation; whereas, no such structural perturbation is noted for the *-indole* group conjugation. Interestingly, both the -COOH and *-indole* interaction sites, showing nearly the same values of small charge transfers, share a common factor of an *indole* group during conjugation with Au₃₂ (Figure 23). The relatively stronger-than-expected interactions from the *indole* group in the computed results occur as a result of the indole group donating a π electron cloud to the Au atoms. The planarity of *indole* also maximizes the delocalization interaction. These effects were observed in previous studies [34]. Thus, our calculation suggests that the preferred nature of the bonding was dominated by π interactions with only a small charge transfer.

Figure 24 shows the charge density plots projected along the 001 plane for all the isomeric configurations of the Trp-Au₃₂ complex (Figure 24b) compare to native Trp and Au₃₂ (Figure 24a). Figure 24b clearly shows that the interaction and charge redistribution are taking place with the *indole* ring and carbonyl oxygen in Trp-Au₃₂ complex for I -COOH group interaction, corroborating previous results. For the II-*indole* group complex in Figure 24b, the charge density plot shows a weak charge delocalization *with the -indole* group, indicating existing π electronic interactions for Trp-Au₃₂ conjugation. The charge density plot for III- -NH_2 in Figure 24b reveals an electronic charge redistribution during -NH_2 group interaction that is higher than the other two mentioned interactions. Hence, charge density results provide evidence for the nature of interactions as predicted in Figure 24.

(a) Total charge density of native Au_{32} and Trp



(b) Total charge density of Trp- Au_{32} complex

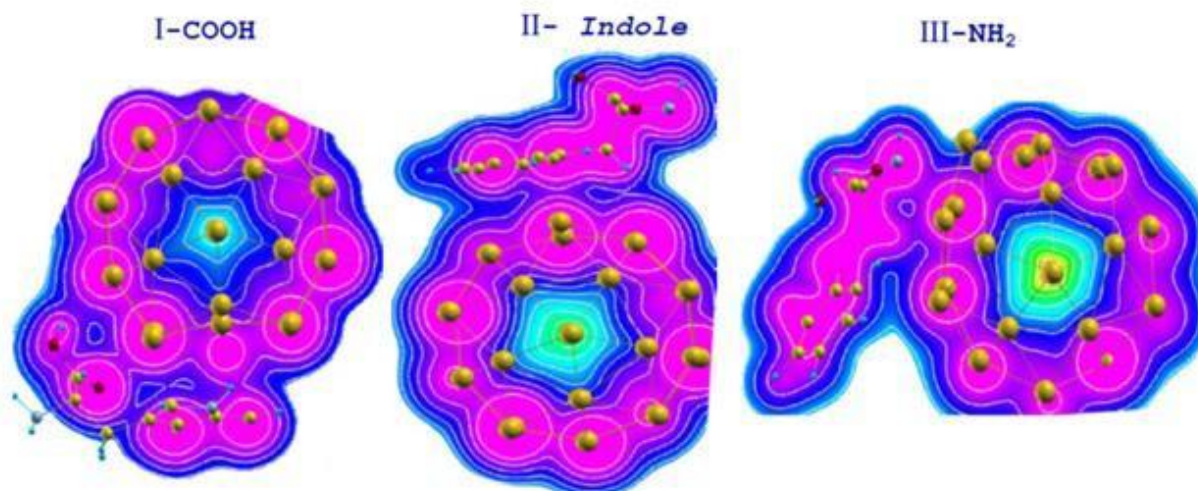


Figure 24. Total charge density plot of Au_{32} , Trp and isomeric configurations of Trp- Au_{32} complex projected along 001 plane. A superimposed ball and stick model identifies the atoms in the complex. Total charge density is shown at 1/3rd of its maximum isosurface value.

The previous experimental study identifies the binding site of Au nanoparticles in BSA containing Trp in near vicinity, resulting in fluorescence quenching [23,24]. Since the spectral signatures of the protein-Au conjugate are dominated by the π - π^* transition of Trp's *indole* functional group, the formation of the complex could modify the electronic states or introduce new states in Trp, resulting in loss of fluorescence energy. In order to examine this, we plotted the highest occupied molecular orbital (HOMO) and lowest unoccupied molecular orbital (LUMO) of the pristine Trp, Au_{32} and Trp- Au_{32} isomers in Figure 25.

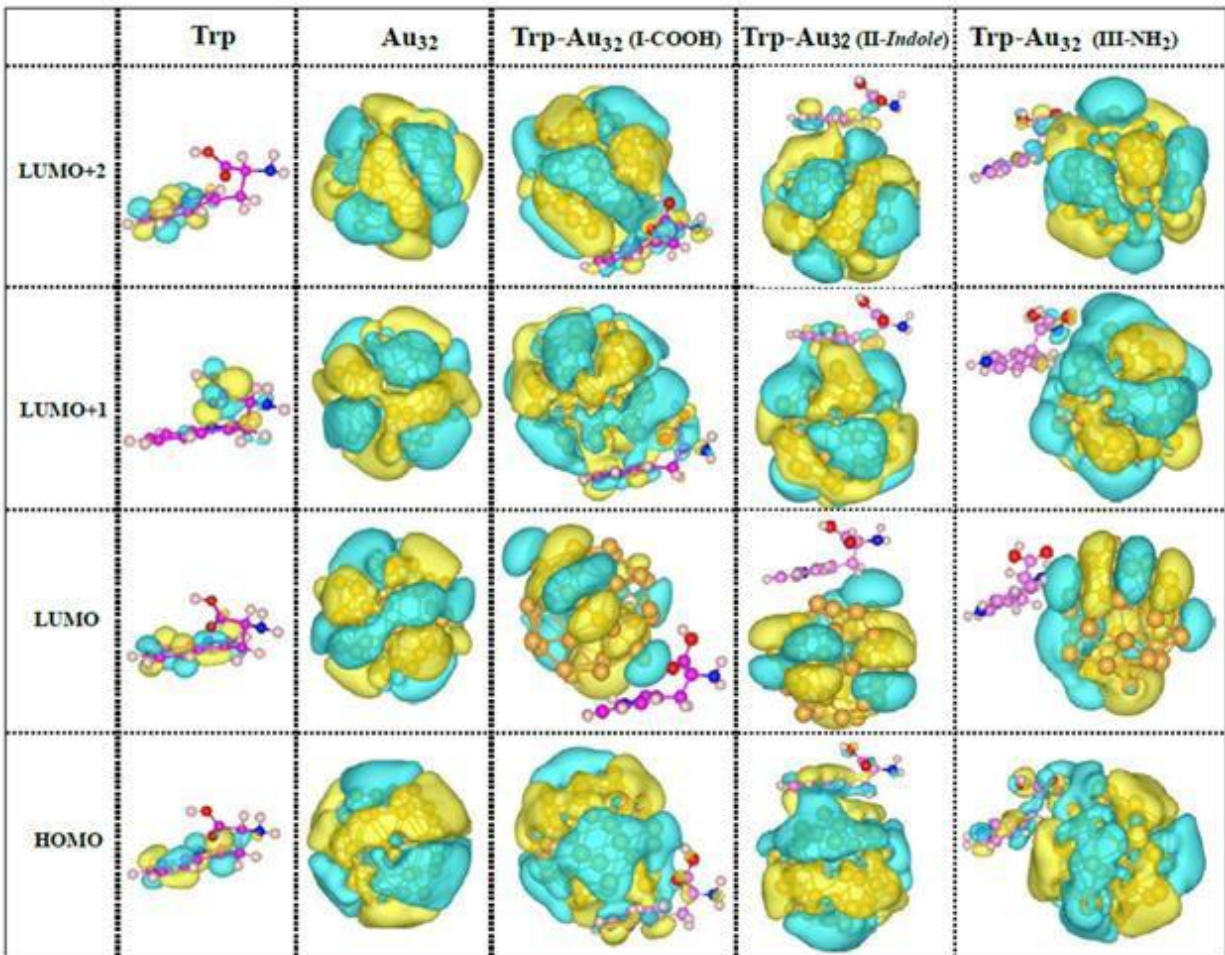


Figure 25. The contour plots of molecular orbitals of pristine Trp, Au₃₂ and Trp-Au₃₂ conjugate isomers shown at 1/2nd of its maximum isosurface value.

As seen in the figure, the HOMO and LUMO of pristine Trp are localized at the *indole* functional group. However, significant modification in the nature of molecular orbitals, and hence the charge re-distribution happens upon the Trp-Au₃₂ conjugate formation. The orbitals associated with Au atoms appear as low-lying LUMO in the energy spectrum of all the three isomers. This LUMO may potentially act as an acceptor from the excited fluorescence state of Trp in the complex, thus reducing the fluorescence intensity. The higher LUMOs i.e. LUMO+1, LUMO+2 are delocalized over Au atoms as well as on the interacting Trp atoms. The delocalized higher LUMOs indicate that the hybridization in Trp-Au₃₂ yields orbitals of a mixed metal-molecule character.

Appearances of Au localized LUMO, hybrid LUMO+1 and LUMO+2 orbitals are further confirmed by the total density of states (DOS) of isomers as shown in Figure 26. The DOS of Trp-Au₃₂ isomers show hybrid states near to Fermi energy that are introduced in the system by Au, which most likely causes fluorescence quenching as measured in our experiments.

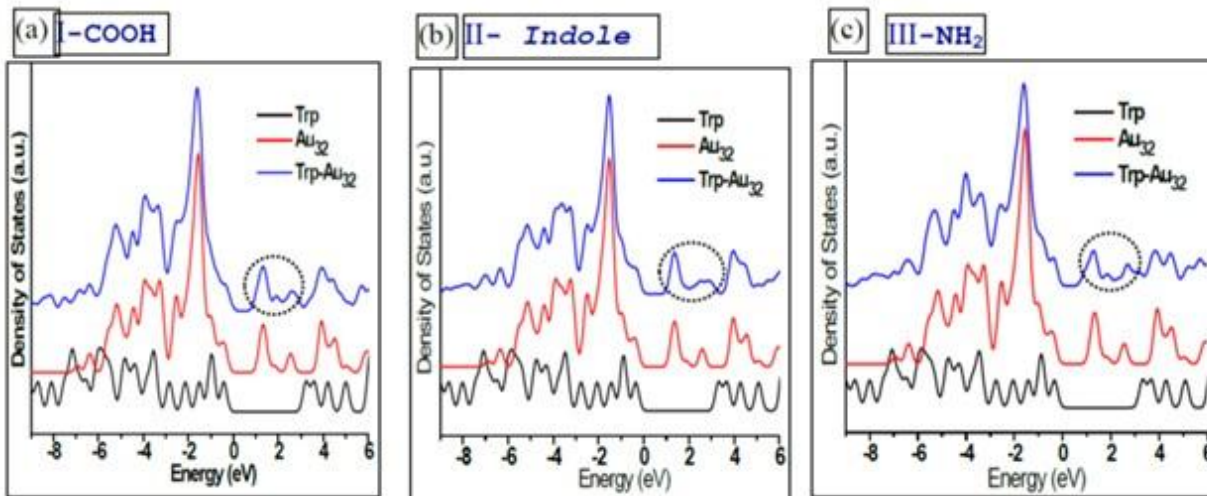


Figure 26. Density of states of Trp, Au₃₂ and Trp-Au₃₂ complex isomers: (a) I-COOH, (b) II-indole and (c) III-NH₂. The HOMO is aligned to origin in energy scale. The low lying hybrid excited states introduced by Au are marked in pink circle.

The aromatic organic molecules are reported to show signatures of weak chemisorption at gold surfaces, producing the bonding- and anti-bonding-like hybrid orbitals below and above the middle of the metal d band, as illustrated in the Newns-Anderson model (Figure 27f) [35]. The model shows that the metal d electron band interacts with highest occupied electron level of the interacting atom and produces bonding and anti-bonding levels. Since the chemisorption is weak, the signatures for these levels are also expected to be weak. Thus, the nature of hybridization at the interacting interface of Trp-Au₃₂ isomers is determined in detail from the computed projected density of states (PDOS).

Figure 27 represents projected density of states (PDOS) centered on atoms involved in the hybridization during Trp-Au₃₂ complex formation, compared to their native state. Figure 27a shows PDOS of native Au d electrons before conjugation, showing strong peaks in the -6 to -2 eV energy range and is apparently localized. Figure 27b shows the p orbitals on native Trp atoms participating in the hybridization. The PDOS of carbon atoms in the *indole* ring are summed up and presented together as *indole* C, while the *indole* nitrogen N1 is shown separately. The structure of Trp with marked atom numbers is shown in Figure 22b. The *indole* carbon atoms show sharp peaks due to the presence of a delocalized π electron cloud in the aromatic ring. The nitrogen atom N1 is also a part of this aromatic π electron system and therefore found to follow the same trend of the *indole* C spectrum with less intensity (Figure 27b). There is a strong peak noted around -1.2 eV, which is attributed to the lone pair of the nitrogen atom N2 of the amine group in Trp. The oxygen O1 also appears with a strong peak around -3.5 eV, related to its lone pairs. The oxygen atom O2 appears with two strong peaks around -3.5 and -2 eV related to its lone pair and carbonyl π electrons respectively.

Figure 27c represents the PDOS of hybridizing atoms of Trp-Au₃₂ complex at -COOH site. Following the Newns-Anderson model, the energy range of -8 to -4 eV is assigned

to the bonding region and -2 to 0 eV is assigned to the anti-bonding region. The peaks corresponding to Au, oxygen O1, oxygen O2, *indole* C and N1 have been modified compared to the initial one in Figure 27b, confirming their participation in hybridization and their contribution to bonding and anti-bonding orbitals. Similar to this, Figure 27d represents the PDOS of the Trp–Au₃₂ complex for the *-indole* interacting site, showing participation of Au, C2, *indole* C and N1 in the hybridization and formation of bonding and anti-bonding peaks from -8 to -4 eV and -2 to 0 eV respectively. Figure 27e shows the PDOS of hybridizing atoms of the Trp–Au₃₂ complex during the *-NH₂* site interaction. The lone pair of N2 has been largely modified as would be expected for this interaction as with O2. The O1 also seems to participate in this interaction, as its orbital signatures have been modified. The anti-bonding region of the hybridizing system in all three interacting site is actually crossed by the fermi level; therefore the region has been found to be less populated. The presence of the underlying broad metal s band affects the nature of hybrid bonding and anti-bonding orbitals and generates spread peaks rather than single localized peaks.

It is clearly demonstrated in the PDOS plots of Trp–Au isomers, that the peak corresponding to the LUMO (~1eV) of the isomer is mainly centered at the interacting Au atoms, though the higher excited levels show a mixed Au–Trp character as evident by molecular orbital (Figure 25) and DOS analyses (Figure 27).

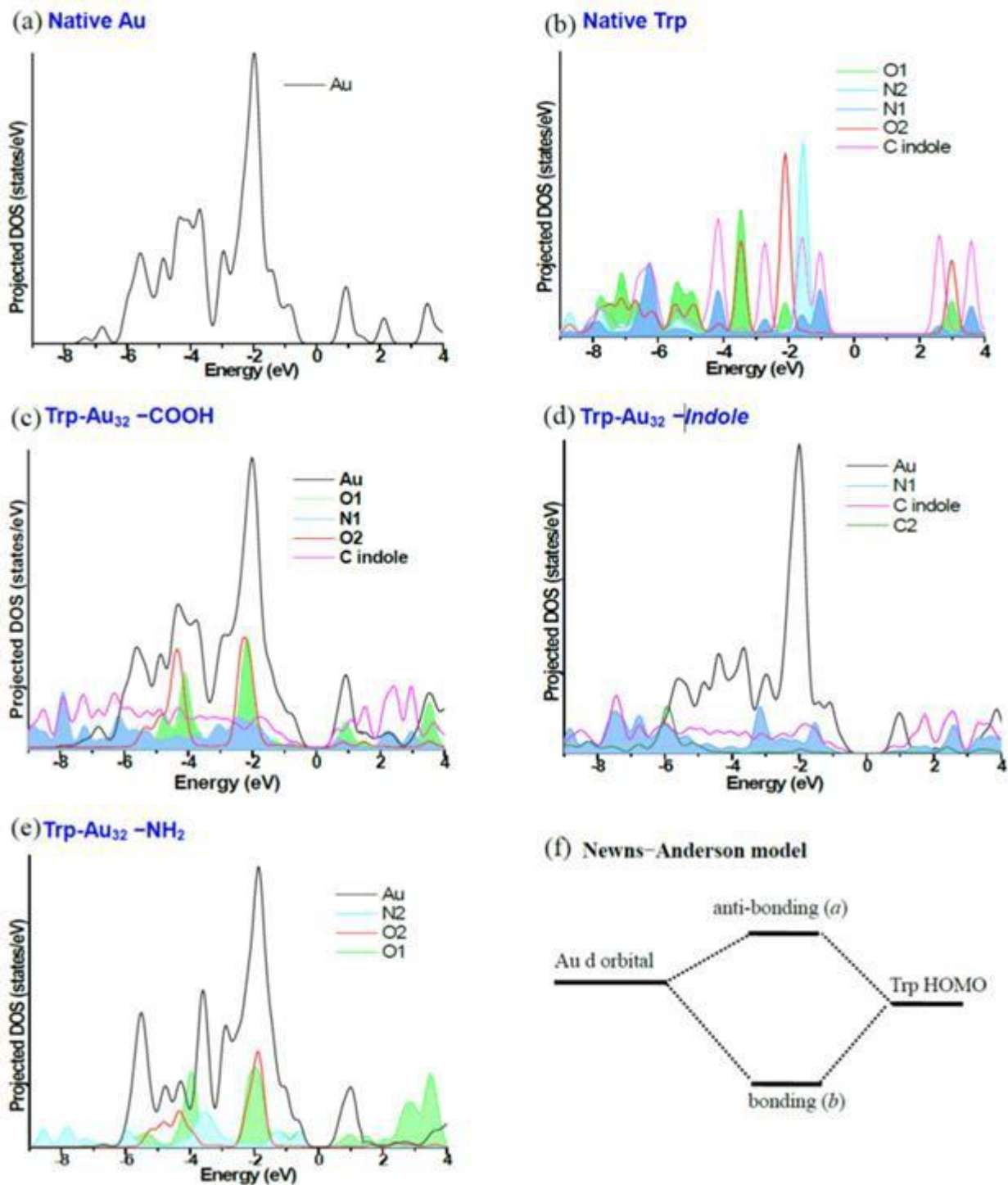


Figure 27. The projected density of states (PDOS) of interacting atoms in (a) native Au₃₂, (b) native Trp, (c) -COOH group, (d) -indole group, (e) -NH₂ group isomers of Trp-Au₃₂ and the (f) Newns-Anderson bonding scheme. Fermi levels are aligned at the origin of the energy scale

Conclusion

First principles calculations based on DFT were performed on Trp, Au₃₂ and Trp–Au₃₂ in order to study the details of the nature of the interaction between tryptophan and gold. We find that preference of the binding involving both carboxyl and *indole* functional groups yielding the mixed salt bridge and charge solvation structure to be energetically more favorable and mediated by stronger-than-expected π interactions offered by the *indole* group. The present study does support the experimental finding of a ground-state Trp–Au complex formation. However, the present study depicts π interactions along with small ionic interactions, instead of van-der Waals between Trp and Au nanoparticles. The hybridization during the formation of the stable Trp–Au complex is anticipated to modify the nature of Trp's molecular orbitals by introducing hybrid states associated with Au as low lying excited states. The PDOS analysis suggests that these hybrid orbitals, produced by the coupling of the narrow Au d band with Trp atomic orbitals have a mixed metal-molecule character and are delocalized at the interface. The non-radiative energy transfer to these states is likely to cause the experimentally observed fluorescence quenching in Trp.

References

- [14] Zhang, L.; Gu, F. X.; Chan, J. M.; Wang, A. Z.; Langer, R. S.; Farokhzad, O. C. *Clinical Pharmacology and Therapeutics* **2008**, *83*, 761–769.
- [15] Chen, P. C.; Mwakwari, S. C.; Oyelere, A. K. *Nanotechnology, Science and Applications* **2008**, *1*, 45–66.
- [16] De, M.; You, C. C.; Srivastava, S.; Rotello, V. M. *J. Am. Chem. Soc.* **2007**, *129*, 10747–10753.
- [17] Lynch, I.; Dawson, K. A. *Nanotoday* **2008**, *3*, 40–47.
- [18] Lacerda, S. H. D. P.; Park, J. J.; Meuse, C.; Pristinski, D.; Becker, M. L.; Karim, A.; Douglas, J. F. *ACS Nano* **2010**, *4*, 365–379.
- [19] Brewer, S. H.; Glomm, W. R.; Johnson, M. C.; Knag, M. K.; Franzen, S. *Langmuir* **2005**, *21*, 9303–9307.
- [20] Du, H.; Fuh, R. A.; Li, J.; Corkan, A.; Lindsey, J. S. *Photochemistry and Photobiology* **1998**, *68*, 141–142.
- [21] Vivian, J. T.; Callis, P. R. *Biophysical Journal* **2001**, *80*, 2093–2109.
- [22] Lindman, S.; Lynch, I.; Thulin, E.; Nilsson, H.; Dawson, K. A.; Linse, S. *Nano Lett.* **2007**, *7*, 914–920.
- [23] Joshi, P.; Chakraborty, S.; Dey, S.; Shanker, V.; Ansari, Z. A.; Singh, S. P.; Chakrabarti, P. *J. Colloid Interface Sci.* **2011**, *355*, 402–409.
- [24] Chakraborty, S.; Joshi, P.; Shanker, V.; Ansari, Z. A.; Singh, S. P.; Chakrabarti, P. *Langmuir* **2011**, *27*, 7722–7731.
- [25] Yin, W. J.; Gu, X.; Gong, X. G. *Solid State Communications* **2008**, *147*, 323–326.
- [26] Joshi, P.; Shewale, V.; Pandey, R.; Shanker, V.; Hussain, S.; Karna, S. P. *Phys. Chem. Chem. Phys.* **2011**, *13*, 476–479.
- [27] Soler, J. M.; Artacho, E.; Gale, J. D.; García, A.; Junquera, J.; Ordejón, P.; Sánchez-Portal, D. *J. Phys.: Condens. Matter* **2002**, *14*, 2745–2779.
- [28] Perdew, J. P.; Burke, K.; Ernzerhof, M. *Phys. Rev. Lett.* **1996**, *77*, 3865–3868.
- [29] Troullier, N.; Martins, J. L. *Phys. Rev. B* **1991**, *43*, 1993–2006.

- [30] Sánchez-Portal, D.; Artacho, E.; Soler, J. M. *J. Phys.: Condens. Matter* **1996**, *8*, 3859–3880.
- [31] Gu, X.; Ji, M.; Wei, S. H.; Gong, X. G. *Phys. Rev. B* **2004**, *70*, 205401–5.
- [32] Crespo, A.; Turjanski, A. G.; Estrin, D. A. *Chem. Phys. Lett.* **2002**, *365*, 15–21.
- [33] The “salt-bridge” and “charge-solvent structure” are used to represent corresponding bonding sites following the nomenclature used in protein chemistry.
- [34] Iori, F.; Felice, R. D.; Molinari, E.; Corni, S. *J. Comput. Chem.* **2009**, *30*, 1465–1476.
- [35] Iori, F.; Corni, S.; Felice, R. D. *J Phys. Chem. C* **2008**, *112*, 13540–13545.

2. Lipid-Nanoparticle Interactions: DMTAP, DMOC and DMPE Bilayers

Introduction

A biological membrane separates a cell from its surrounding environment, and its function depends on the continuity and integrity of the bilayer structure, since over 70% weight of membrane belong to a lipid bilayer [36]. Consequently, knowledge of the structure of a lipid bilayer is the key element to understand the functionality of a biological membrane, especially the tertiary structure which can be obtained by the X-ray diffraction measurements [37-43].

In recent years theoretical methods have become one of the important tools to investigate the physical properties of a biological system. These methods are generally based on molecular dynamics (MD) and Monte Carlo (MC) methods, and can provide three-dimensional real-time imaging of the complex biological system and simulate many important phenomena including self-assembly, phase transition [43-49], and lipid-molecule interactions [50-55], and the lipid bilayer system [56-62]. We note that these atomistic simulation methods are quite limited when it comes to obtaining the electronic structure of lipid bilayers. Furthermore, their accuracy depends on the description of the force field parameters obtained by the empirical methods.

In this study, we employ an alternative way of calculating both structural and electronic properties of lipid bilayers which does not require the knowledge of the force field parameters. Our first-principles method is based on density functional theory. Recently, Mashaghi and co-workers used first principles method to investigate hydration affection on molecular and electronic structure of phospholipid [63]. It is to be noted here that the overall aim of this project is to investigate interactions between nanoparticles and cell membranes, which are central to understanding the potential deleterious effects of nanoparticle on living cells.

Computational method

Since calculations based on first principles methods are computationally intensive, our challenge will be how to simplify the lipid bilayer structure for simulation without losing its essential structural features which are important in the understanding of its functioning. Assuming a 2-dimensional periodic structure of the lipid layer, we employed the framework of the generalized gradient approximation (GGA) to density functional theory using the Vienna ab initio Simulation Package (VASP). The projector augmented-wave (PAW) [64-67] potentials and plane wave basis sets together with the exchange and correlation functional forms proposed by Perdew and Zunger [69,70] were used. During the optimization procedure, the size of the super cell as well as the internal coordinates of all the atoms was relaxed. The energy cutoff of the plane wave was taken to be 400 eV.

Results and Discussion

DMTAP (Figures 28 and 29) belongs to a class of double-chained cationic lipid amphiphiles, and has shown considerable promise as potentially effective DNA transfection agents. The lipid structure has, in general, two types of chemical groups. One chemical group brings the positive charge such as the choline, amine etc., whereas the negative charge is associated with the phosphate group. All of the positive charges in the lipid layer lie on a plane or shell, and all of the negative charges lie in the other plane or shell. These two charge plane or shells make up the electric double layer which mainly determines the functionality of a cell membrane.

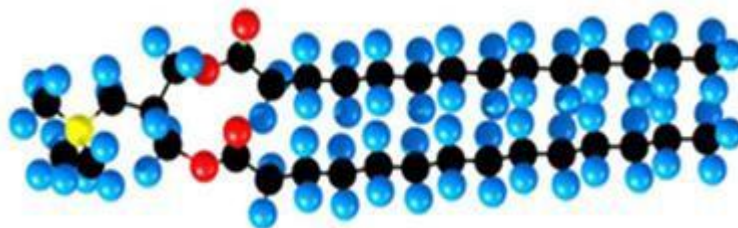


Figure 28. A ball and stick model for DMTAP (O : red, C : gray , N: yellow, H : blue)

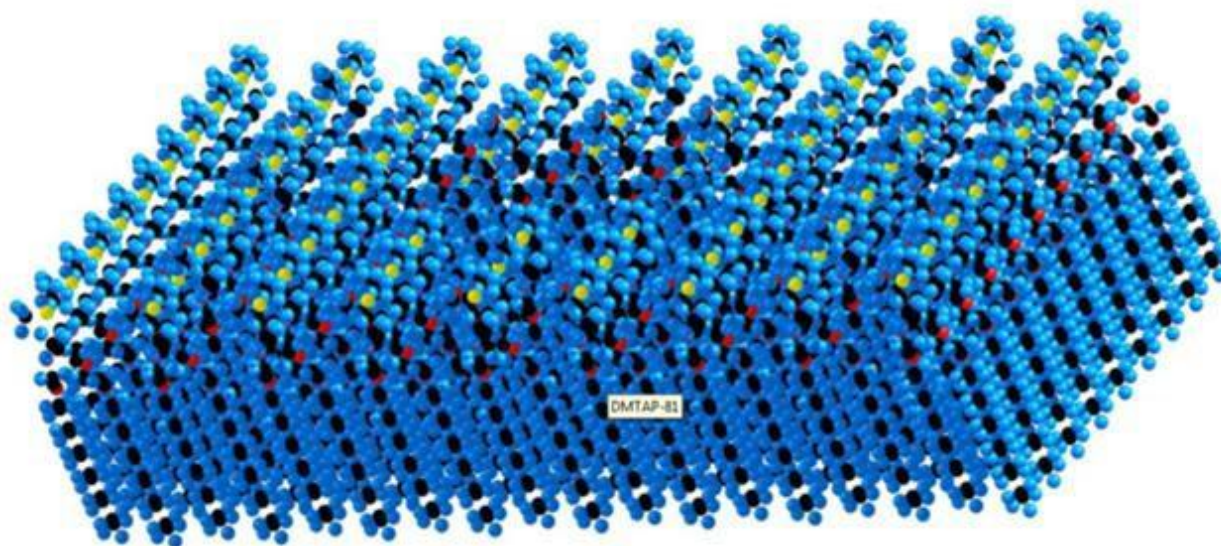


Figure 29. A ball and stick model for DMTAP layer. (O : red, C : gray , N: yellow, H : blue)

In our simulation model, the super cell of the DMTAP lipid layer has a triclinic Bravais Lattice. The average area per lipid molecule is calculated as follows:

$$A = b \times c \times \sin \alpha$$

The calculated values of the parameters for the optimized DMTAP unit cell and the experimental results [70] are shown in Table 11.

Table 11. The calculated structural properties of DMTAP.

	b (Å)	c (Å)	α (°)	Area/lipid (Å ²)	Volume (Å ³)
This work	4.4	8.0	96.2	34.9	904
Experiment [36]	5.1	7.3	92	37	917

We note that the average area per lipid is one of most fundamental characteristics of lipid bilayers. The excellent agreement between our calculated results with the experimental value successfully validates the modeling elements employed.

The lipid bilayers, phosphatidylcholine (PC) and phosphatidylethanolamine (PE), represent the abundant phospholipids class in animal and plant tissues, and can be the major lipid class in microorganisms. In the present study, we take 1,2-Dimyristoyl-sn-glycero-3-phosphorylcholine (DMPC) and 1,2-Dimyristoyl-sn-glycero-3-phosphorylethanol- amine (DMPE) as the representative members of the PC and PE types shown in Figures 30 and 31. Note that the difference between the PE and PC is the N atom in the hydrophilic head – it is connected to three methyl groups in DMPC, but is connected to three H atoms in DMPE.

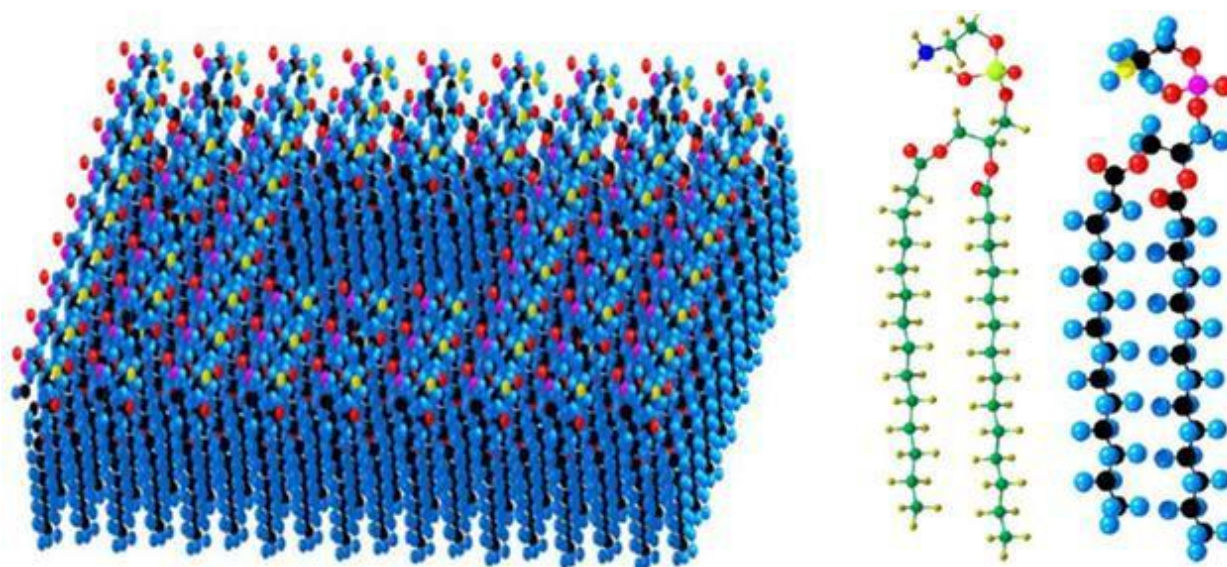


Figure 30. A ball and stick model for DMPC layer. (O : red, C : gray , N : yellow, H : blue)

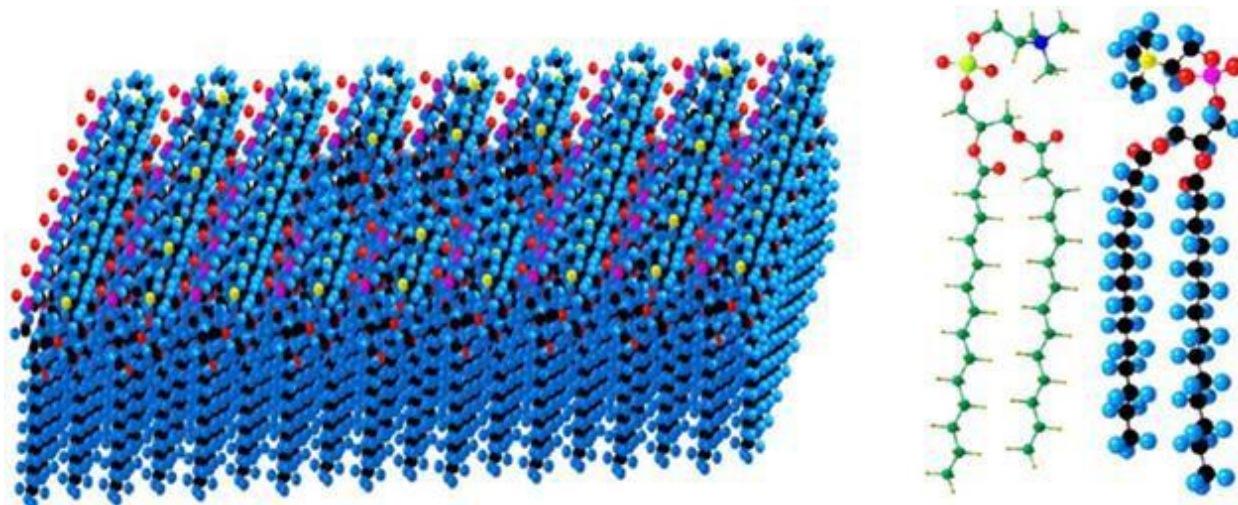


Figure 31. A ball and stick model for DMPE layer. (O : red, C : gray , N : yellow, H : blue)

In order to make calculations computationally feasible, we first performed calculations to investigate the number of C atoms required to represent the “tail” of a fatty acid, which was a long hydrocarbon chain. Table 12 lists the results of such calculations where we find that the area associated with 8 C atoms representing the "tail" of the fatty acid was reasonably enough for further simulation of DMPC and DMPE. This was consistent with the experimental study which reported the average area per lipid molecule remains nearly the same for the long hydrocarbon chain.

Table 12. The average area per lipid molecule as a function of number of C atoms representing the "tail" of a fatty acid. Units are in \AA^2 .

C atoms representing the "tail"	DMPC Area/lipid (\AA^2)	DMPE Area (\AA^2)
2	33.60	32.49
4	36.97	33.88
8	37.43	35.64
10	37.62	36.50
14	37.60	39.70

Table 13. The calculated structural properties of DMPC and DMPE.

	b (\AA)	c (\AA)	α ($^\circ$)	Area/lipid(\AA^2)	Volume (\AA^3)
DMPC: This work	4.4	8.6	95.1	37.6	954.1
DMPC: Experiment[37]	4.71	8.46	90.0	39.8	-
DMPE: This work	4.29	9.26	93.1	36.5	1154.9
DMPE Experiment [38]	3.73	9.70	90.0	36.1	-

Both the DMPC and DMPE can be represented by the triclinic Bravais lattice whose parameters are given in Table 13. Considering that the area per lipid becomes smaller

as the temperature decreases [72, 73], the calculated value at 0K follows the trend as the experimental value was obtained at 283K. A comparison between the calculated and experimental values of the lattice parameters shows a good agreement for the lipid layers considered. We note that the previous calculations using the MD method generally found reported the per-area to be 50-60 Å² for DMPC and DMPE lipid bilayers at the low temperature [71].

It is well known that many of the physical and chemical properties of a lipid bilayer can be determined *via* knowledge of the electron density. Figures 32 and 33 show the electron density contour plots of the electric double layer part of DMPC and DMPE, respectively.

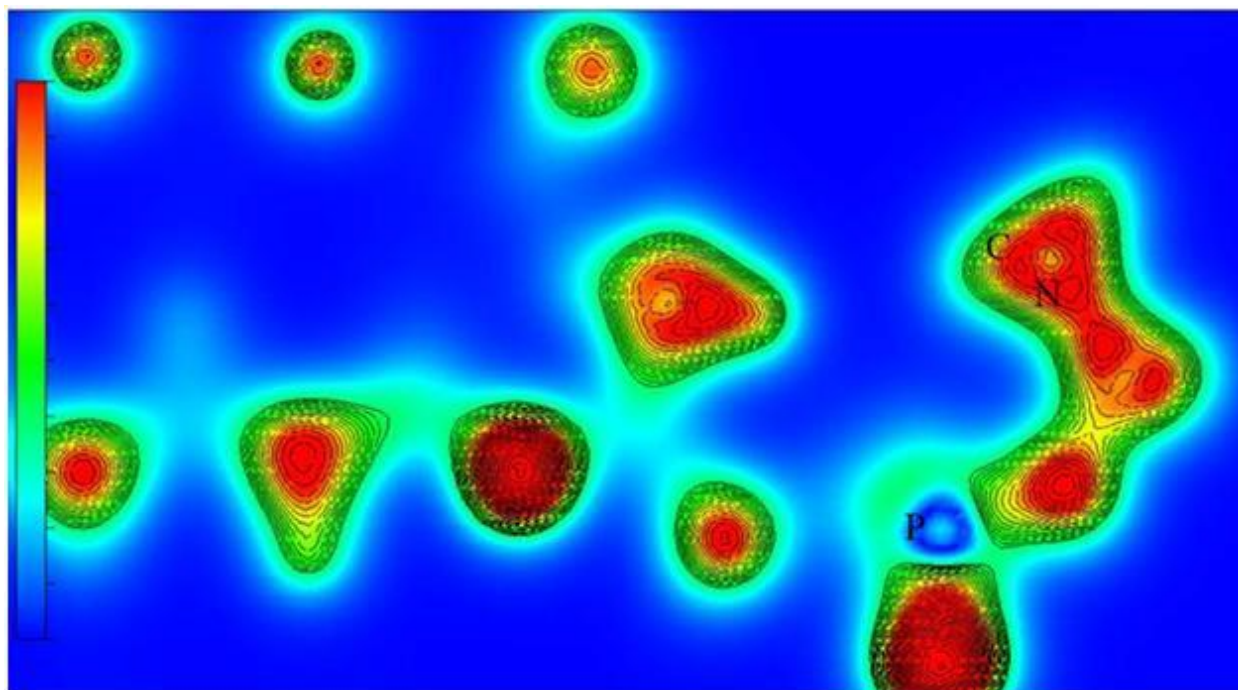


Figure 32. The electron density contour plots of DMPC.

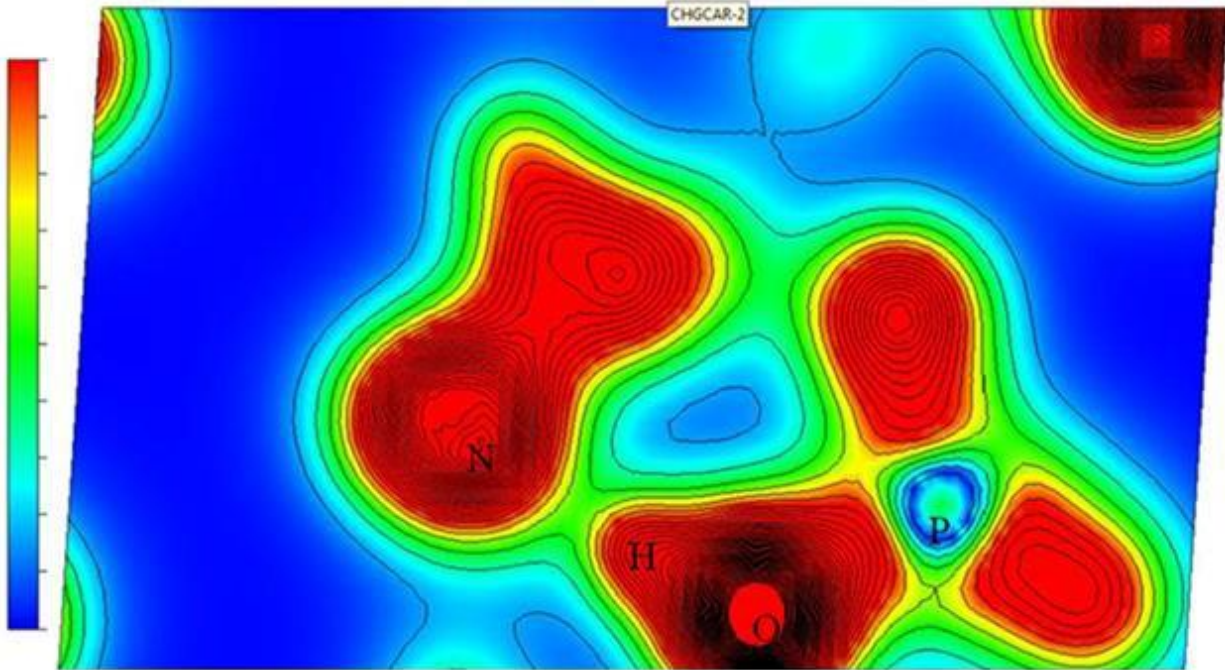


Figure 33. The electron density contour plots of DMPE.

In these systems, the contour plots show that P has lost the electron density to nearby oxygens. On the contrary, N is more electronegative than C, thus the region near N atoms shows excess in the electron density.

In order to mimic the cell live environment, we now add the water molecules in our simulation model for DMPC and DMPE. The corresponding optimized structures of lipid monolayers are shown in Figures 34 and 35.

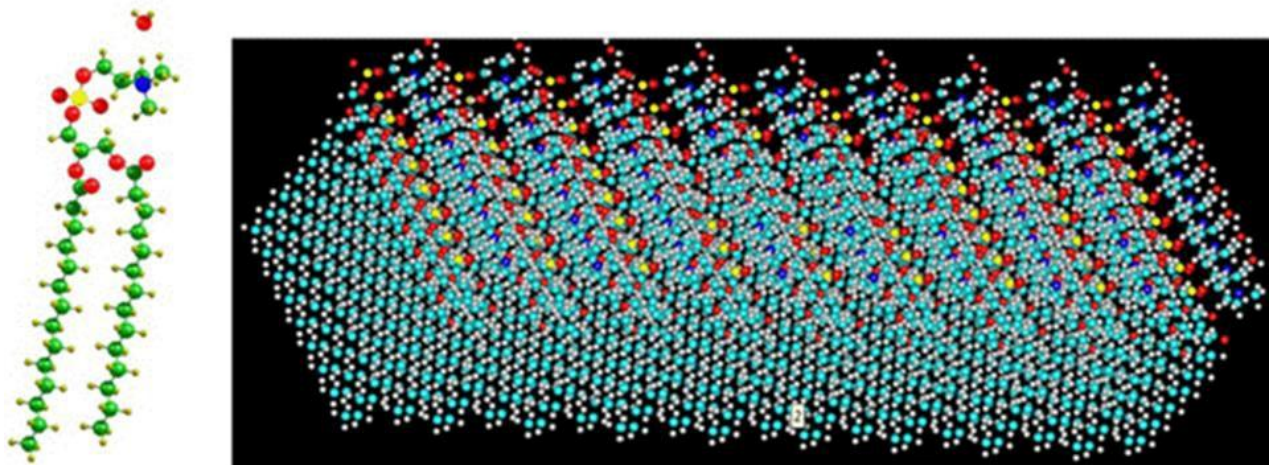


Figure 34. A ball and stick model for the DMPC: H₂O system.
(O: red, C: green, P: yellow, N: blue H: golden)

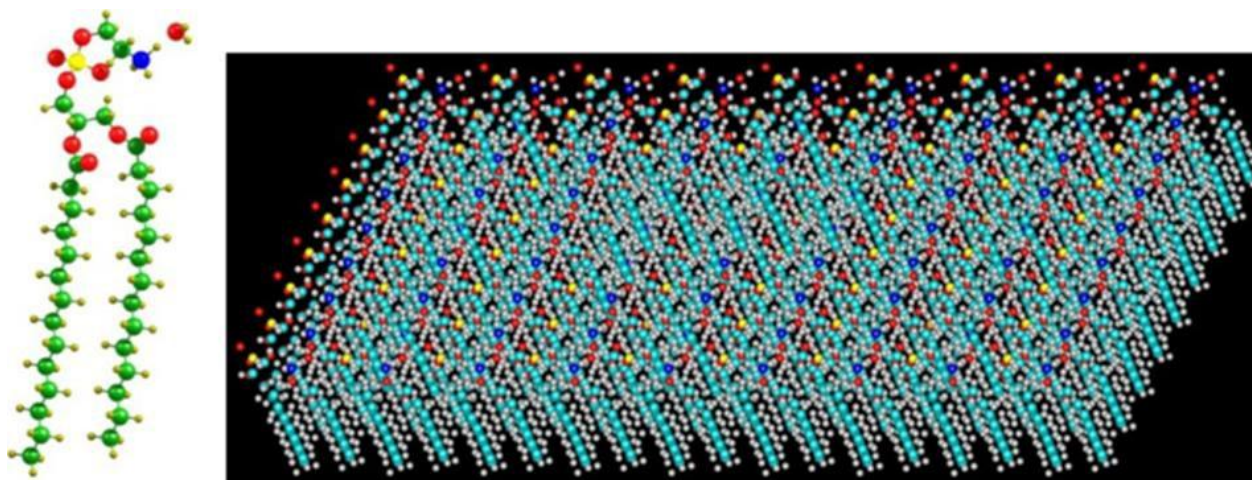


Figure 35. A ball and stick model for the DMPC: H₂O system.
(O: red, C: green, P: yellow, N: blue H: golden)

For a lipid bilayer, the magnitude of the electric dipole moment mainly determines the degree of activity of the membrane [74, 75]. For DMPC and DMPE systems, the calculated values are tabulated in Table 14 considering the center of cell to be (0.5, 0.5, 0.5) as the reference of point.

Table 14. The calculated dipole moments of DMPC and DMPE monolayers.

		α (e \times Å)	β (e \times Å)	γ (e \times Å)	Energy (eV)
DMPC	isolated	-0.851	0.115	-2.561	0.0286
	hydrated	-0.842	0.123	-2.544	0.0283
DMPE	isolated	-0.082	0.011	-1.032	0.0042
	hydrated	-0.411	0.015	-3.184	0.0424

For the bilayer system, our calculated values will be -1.32 and -0.78 kcal/mol for DMPC and DMPE, respectively. A theoretical study using the linearized Poisson-Boltzmann equation reported the value of the electrostatic potential at the bilayer mid-plane to be -1.21, for DMPC bilayer [74, 75]. Furthermore, the results find the presence of the water molecules to be the determining factor in stabilizing the functioning structure of the DMPE bilayer, and facilitates a significantly large change in the dipole moment along the γ direction. The results therefore predict a relatively high activity of the hydrated lipid layer of DMPE relative to that of DMPC for nanoparticles.

Conclusion

Considering that understanding of the interactions between nanoparticles and a biomembrane is central to predict the potential deleterious effects of nanoparticle on living cells, we performed simulation of lipid bilayers using first principles methods. The

calculated results show, for the first time, the accuracy and reliability of such methods in calculating the structural property of for DMTAP, DMPC and DMPE bilayer systems. We also examine the solvation effects, and find that the presence of the water molecules is essential in stabilizing the configuration of the DMPE bilayer. It also facilitates a significantly large change in its dipole moment along the γ direction. The results therefore predict a relatively high activity of the hydrated lipid layer of DMPE relative to that of DMPC for nanoparticles.

References

- [36] Wuthier, R.E. *J. Lipid Res.* **1966**, *7*, 544
- [37] Lyubartsev, A.P.; Rabinovich, A.L. *Soft Matter* **2011**, *7*, 25.
- [38] Elder, M., et al. *Proc. R. Soc. London A.* **1977**, 354.
- [39] Pearson, R H.; Pascher, I. *Nature* **1979**, *281*, 499.
- [40] Vanderkooi, G. *J. Phys. Chem.* **1990**, *94*, 4366.
- [41] Hauser, H. J. *Mol. Bio.* **1980**, *37*, 249.
- [42] Wu, Y.; He, K.; Ludtke, S.J.; Huang, H.W. *J. Biophysical.* **1995**, *68*, 2361.
- [43] Wiener, M.C.; White, S.H. *J. Biophysical.* **1992**, *61*, 434.
- [44] Scott, K.A.; Bond, P.J.; Ivetac, A.; Chetwynd, A.P.; Khalid, S; Sansom, M.S.P. *Structure* **2008**, *16*, 621-630.
- [45] Monnard, P-A.; Deamer, D.W. "Membrane Self-Assembly Process: Steps Toward the First Cellular Life", Part II, Chapter 8 in *The Minimal Cell: The Biophysics of Cell Compartment and the Origin of Cell Functionality* **2011**, 123.
- [46] Farago, O.; Grønbech-Jensen, N. *J. Am. Chem. Soc.* **2009**, *131*, 2875.
- [47] Saksena, R.S.; Coveney, P.V. *J. Phys. Chem. B* **2008**, *112*, 2950.
- [48] Nishizawa, M.; Nishizawa, K. *J. Biophys. Chem.* **2010**, *1*, 19.
- [49] Giner Casares, J.J.; Camacho, L.; Martín Romero, M.T.; López Cascales, J. J. *J. Phys. Chem. B* **2007**, *111*, 13726.
- [50] López Cascales, J.J.; Otero, T.F.; Fernández Romero, A.J.; Camacho, L. *Langmuir* **2006**, *22*, 5818.
- [51] Wong-Ekkabut, J.; Baoukina, S.; Triampo, W.; Tang, I-M.; Tieleman, D.P.; Monticelli, L. *Nature Nanotechnol.* **2008**, *3*, 363.
- [52] Villarreal, M.A.; Díaz, S.B.; Disalvo, E.A.; Montich, G.G. *Langmuir* **2004**, *20*, 7844.
- [53] Bedrov, D.; Smith, G.D.; Davande, H.; Li, L. *J. Phys. Chem. B* **2008**, *112*, 2078.
- [54] Li, L.; Davande, H.; Bedrov, D.; Smith, G.D. *J. Phys. Chem. B* **2007**, *111*, 4067.
- [55] Rozario, R.S.G.D.; Wee, C.L.; Wallace, E J.; Sansom, M.S.P. *Nanotechnology* **2009**, *20*, 1.
- [56] Liu, J.; Hopfinger, A.J. *Chem. Res. Toxicol.* **2008**, *21*, 459.
- [57] Biggin, P.C. ; Sansom, M.S.P. *Biophys.Chem.* **1999**, *76*, 161.
- [58] Chiu, S-W.; Subramaniam, S.; Jakobsson, E. *Biophys. J.* **1999**, *76*, 1929.
- [59] Bond, P.J.; Sansom, M.S.P. *Mol. Membr. Biol.* **2004**, *21*, 151.
- [60] La Rocca, P.; Biggin, P.C.; Tieleman, D.P.; Sansom, M.S.P. *Biophysica Acta* **1999** *1462*, 185.
- [61] de Planque, M.R.R.; Killian, J. A. *Mol. Membr. Biol.* **2003**, *20*, 271.
- [62] Boggara, M.B.; Krishnamoorti, R. *Biophysical J.* **2010**, *98*, 586.
- [63] Sansom, M.S.P.; Scott, K.A.; Bond, P.J. *Biochem Soc Trans.* **2008**, *36*, 27.

- [64] Mashaghi, A.; Partovi-Azar, P.; Jadidi, T.; Nafari, N.; Maass, P.; Tabar, M.R.R., Bonn, M.; Bakkar, H.J. *J. Chem. Phys.* **2012**, *136*, 114709.
- [65] Park, K.; Lee, D.; Rai, A.; Mukherjee, D.; Zachariah, M.R. *J. Phys. Chem. B* **2005**, *109*, 7290.
- [66] Kresse, G.; Furthmüller, J. *Phys. Rev. B* **1996**, *54*, 11169 .
- [67] Blöchl, P.E. *Phys. Rev. B* **1994**, *50*, 17953.
- [68] Kresse, G.; Joubert, D. *Phys. Rev. B* **1999**, *59*, 1758.
- [69] Perdew, J.P.; Zunger, A. *Phys. Rev. B* **1981**, *23*, 5048.
- [70] Perdew, J.P.; Chevary, J.A.; Vosko, S.H.; Jackson, K.A.; Pederson, M.R.; Singh, D.J.; Fiolhais, C. *Phys. Rev. B* **1992**, *46*, 6671.
- [71] Gurtovenko, A. A.; Patra, M.; Karttunen, M.; Vattulainen, I. *Biophys. J.* **2004**, 3461.
- [72] Wiener, M.C.; Suter, R.M.; Nagle, J.F. *Biophys. J.* **1989**, *55*, 315.
- [73] Suwalsky, M.; Duk, L. *Makromol. Chem.* **1987**, *188*, 599.
- [74] Zheng, C.; Vanderkooi, G. *J. Biophys.* **1992**, *63*, 935.
- [75] Gabdouliline, R. R. Zheng, C. Vanderkooi, G. *Chem. Phys. Lipids* **1996**, *84*, 139.

Acknowledgment:

Helpful discussion with Chunhui Liu and Haiyng He are acknowledged.

Section IV.

Publications

A. ACCEPTED PUBLICATIONS:

Mukhopadhyay A.; Grabinski, C.M.; Saleh, N.; Hussain, S.M. Effect of surface chemistry of gold nanospheres on protein adsorption and cell uptake *in vitro*. *Applied Biochemistry and Biotechnology* **2012**, *167*, 327-337.

Schaeublin, N.M.; Braydich-Stolle, L.K.; Maurer, E.I.; Park, K.; Maccuspie, R.I.; Afrooz, A.N.; Saleh, N.B.; Vaia, R.A.; Hussain, S.M. Does shape matter? Bioeffects of gold nanomaterials in a human skin cell model. *Langmuir* **2012**, *28*, 3248-3258.

Joshi, P.; Shewale, V.; Pandey, R. Tryptophan-gold nanoparticle interaction: A first-principles quantum mechanical study. *Journal of Physical Chemistry C* **2011**, *115*, 22818-22826.

Comfort, K.K.; Maurer E.I.; Braydich-Stolle, L.K.; Hussain, S.M. Interference of silver, gold, and iron oxide nanoparticles on epidermal growth factor signal transduction in epithelial cells. *ACS Nano* **2011**, *5*, 10000-10008.

Nishanth, R.P.; Jyotsna, R.G.; Schlager, J.J.; Hussain, S.M.; Reddanna, P. Inflammatory responses of RAW 264.7 macrophages upon exposure to nanoparticles: role of ROS-NFκB signaling pathway. *Nanotoxicology*, **2011**, *5*, 502-516.

Trickler, W.J.; Lantz, S.M.; Murdock, R.C.; Schrand, A.M.; Robinson, B.L.; Newport, G.D.; Schlager, J.J.; Oldenburg, S.J.; Paule, M.G.; Slikker, W. Jr.;

- Hussain, S.M.; Ali, S.F. Brain microvessel endothelial cells responses to gold nanoparticles: In vitro pro-inflammatory mediators and permeability. *Nanotoxicology* **2011**, *5*, 479-492
- Schaeublin, N.M.; Braydich-Stolle, L.K.; Schrand, A.M.; Miller, J.M.; Hutchison, J.; Schlager, J.J.; Hussain, S.M Surface charge of gold nanoparticles mediates mechanism of toxicity. *Nanoscale* **2011**, *3*, 410-420.
- Sharma, M.; Salisbury, R.L.; Maurer, E.; Hussain, S.M.; Sulentic, C.E.W. Gold nanoparticles induce transcriptional activity of NF- κ B in a B-lymphocyte cell line. *Accepted to Nanoscale*.

B. PUBLICATIONS IN PREPARATION:

- Schaeublin, N.M.; Maurer, E.I.; Gajewicz, A.; Puzyn, T.; Leszczynski, J.; Hussain, SM. Application of QSAR modeling to predict metal nanoparticle toxicity. *In progress*.
- Grabinski, C.M.; Sankaran, R.M.; Hussain, S.M. Dosimetry considerations for *in vitro* toxicity of aerosolized nanomaterials at the air liquid interface. *In progress*.
- Grabinski, C.M.; Salaklang, J.; Garrett, C.; Schrand, A.; Hussain, S.; Hofmann, H. Multi-functionalized SPIONs for nuclear targeting applications. *In progress (to be submitted to Nano)*.

C. ABSTRACTS AND PRESENTATIONS

- Grabinski, C.M.; Sankaran, R.M.; Hussain, S.M. Design of an In Vitro Chamber to Study Realistic Occupational Exposure of Engineered Nanomaterials: Poster presented at: Toxicology and Risk Assessment Annual Meeting; 2012 Apr 13; Cincinnati, OH.
- Awarded Best Poster Presentation (sponsored by the meeting) and Best Abstract (sponsored by the Ohio Valley Society of Toxicology)
- Grabinski, C.M.; Sankaran, R.M.; Hussain, S.M. Design of an In Vitro Chamber to Study Realistic Occupational Exposure of Engineered Nanomaterials: Poster presented at: Society of Toxicology Annual Meeting; 2012 Mar 13; San Francisco, CA.
- Schaeublin, N.M.; Maurer, E.I.; Gajewicz, A.; Puzyn, T.; Leszczynski, J.; Hussain, S.M. Application of QSAR Modeling to Predict Metal Nanoparticle Toxicity. Poster presented at: Society of Toxicology Annual Meeting; 2012 Mar 13; San Francisco, CA.
- Grabinski, C.M.; Sankaran, R.M.; Hussain, S.M. Design of an In Vitro Chamber for Occupational Exposure Assessment of NMs: 2012 Jan 10; Talk presented at: ENM EHS meeting; Dayton, OH.

Grabinski, C.M.; Sankaran, R.M.; Hussain, S.M. In Vitro Chamber to Study Realistic Occupational Exposure of Engineered Nanomaterials to Biological Systems. Poster session presented at: Ohio Valley Society of Toxicology: 2011 September 19; Dayton, OH.

Turner, B.; Grabinski, C.M.; Hussain, S. Kinetics of Fluorescent Nanoparticles in an Airway Tissue Model. Poster session presented at: Human Effectiveness Summer Intern Research Presentation Day; 2011 Aug 16; Dayton, OH.

Grabinski, C.M.; Sankaran, R.M.; Hussain, S.M. Portable In Vitro Chamber to Study Realistic Occupational Exposure of Engineered Nanomaterials to Biological Systems. Poster session presented at: Air Force Medical Services Conference: 2011 August 1-4; Washington D.C.